Title:

Hybrid broadband ground-motion simulation using neural networks with spatial, inter-period, and cross-component correlations

Authors:

Victor M. Hernández-Aguirre[1]

Rajesh Rupakhety[1]

Roberto Paolucci[2]

Manuela Vanini[2]

Chiara Smerzini[2]

[1] Earthquake Engineering Research Centre, Faculty of Civil and Environmental Engineering, University of Iceland, Austurvegur 2a, 800 Selfoss, Iceland

Email: victorh@hi.is

[2] Department of Civil and Environmental Engineering, Politecnico di Milano, Milan, Italy

Preprint Statement

This manuscript is a preprint and has not undergone peer review.

The manuscript is currently under review in Earthquake Engineering & Structural Dynamics.

This version is posted on EarthArXiv to ensure transparency, accessibility, and timely dissemination of the research.

The final published version, if accepted, may differ from this preprint.

Date of Preprint Posting:

9 March 2026

V.M. Hernández-Aguirre
victorh@hi.is

[1] Earthquake Engineering Research Center, University of Iceland, Selfoss, Iceland

[2] Department of Civil and Environmental Engineering, Politecnico di Milano, Milan, Italy

Hybrid broadband ground-motion simulation using neural networks with spatial, inter-period, and cross-component correlations

Victor M. Hernández-Aguirre[1] · Rajesh Rupakhety[1] · Roberto Paolucci[2] · Manuela Vanini[2] · Chiara Smerzini[2]

Abstract: Simulated ground motions are increasingly used in earthquake engineering, particularly in regions with sparse strong-motion recordings where constraining non-ergodic ground-motion models (GMMs) remains challenging. Physics-based simulations (PBS) can reproduce key source and wave-propagation effects but are often limited to low frequencies, whereas stochastic methods are computationally efficient but typically lack physically coherent three-component behaviour and realistic near-fault features. Here we develop a hybrid broadband framework with three main innovations (i) an enhanced artificial neural network (ANN) that predicts short-period spectral accelerations (SAs) from long-period PBS SAs and scalar source-site predictor variables, while jointly modelling the three ground-motion components, (ii) a transfer learning strategy that enables regional calibration in data-limited settings, and (iii) an explicit multivariate correlation model for within-event residuals that introduces realistic broadband dependence jointly across space, periods, and components. The approach is evaluated using regional 3D PBS of the M_w 6.5 and M_w 6.4 June 2000 South Iceland earthquakes. For this case study, the resulting broadband fields reproduce observed short-period attenuation and near-fault saturation, are consistent with local Icelandic GMM trends, and preserve physically plausible directionality and component ratios, including spatially varying FN/FP patterns and V/H ratios consistent with empirical models. Inter-period correlations of within-event residuals follow established empirical trends and, importantly, remain continuous across the stochastic–PBS transition, while spatial correlation ranges are comparable to published observations. Owing to its computational efficiency, the framework provides a practical basis for generating spatially and spectrally coherent broadband ground-motion fields for scenario-based hazard and risk applications.

Keywords: Physics-based numerical simulations; machine learning; transfer-learning; broadband ground-motion simulation; ground-motion correlation.

1 Introduction

Simulated ground motions have become increasingly important in earthquake engineering practice, particularly in regions with sparse instrumental strong-motion records or limited coverage of near-fault observations. In such settings, constraining non-ergodic ground-motion models (GMMs), especially in the near field and for large magnitudes, remains challenging. Ground-motion simulation approaches are commonly classified into three categories: deterministic, stochastic, and hybrid.

Deterministic approaches, often referred to as physics-based simulations (PBS), solve the elastodynamic equations to model seismic wave propagation from the source to the site of interest. PBS can reproduce key physical phenomena such as near-fault directivity and the effects of topography and complex site conditions. However, their computational cost and the difficulty of accurately characterizing source complexity and 3-D regional structure often limit their ability to reproduce high-frequency ground-motion content. Consequently, PBS are frequently applied up to about 2–3 Hz, although successful applications extending to ~8 Hz have been reported [1–3]. This can constrain their use in earthquake engineering applications, such as structural analyses and risk assessment studies, that typically require realistic ground-motion characteristics up to about 10 Hz.

Stochastic simulation methods have their basis in the work of Hanks and McGuire [4], who combined seismological models of the spectral amplitude of ground motion with the engineering notion that high-frequency motions are essentially random. Finite-fault implementations are widely used for simulating large-magnitude events, typically by subdividing the fault into sub-sources and summing their contributions with appropriate time delays [5]. Each sub-source is modelled as a point-source producing a signal represented by band-limited white Gaussian noise shaped by source, path, and site effects [6]. Although stochastic methods are computationally efficient, they exhibit limitations, notably in capturing directivity and in producing physically coherent three-component seismograms [7].

Hybrid methods leverage the strengths of physics-based low-frequency (LF) simulations and extend their frequency content by merging LF ground motions with high-frequency components generated using computationally efficient techniques. Examples include using stochastic ground motions [8], Green's functions computed using 1D models with a site-effect correction [9], semi-analytical/semi-numerical source-to-site procedures combining frequency–wavenumber and spectral-element methods [10], and machine-learning approaches [11–14]. Recent machine-learning (ML) assisted hybrid methods have also combined 3D PBS with ANN models to predict broadband surface ground-motion parameters from bedrock simulations and site information [14]. These developments demonstrate the increasing role of hybrid and data-driven strategies in broadband ground-motion simulation. However, most existing hybrid approaches focus primarily on extending the frequency content or predicting marginal intensity measures, whereas fewer methods explicitly address the joint spatial, inter-period, and cross-component dependence required for spatially distributed engineering applications.

Earthquake recordings show that ground-motion intensity measures exhibit both spatial correlation and inter-period (inter-frequency) correlation. Over the past decades, numerous studies have investigated the spatial correlation of response spectra [15–18], as well as inter-period correlations in response spectra and inter-frequency correlations in Fourier spectra [19–25]. Several works have also shown that neglecting these correlations can bias risk estimates, typically leading to an underestimation of seismic risk [22,26–28]. Although PBS inherently include realistic spatial correlation of LF motion arising from source and path effects [29,30], many stochastic and hybrid simulation methods do not provide realistic broadband (BB) spatial and/or inter-period correlation, or exhibit artificial loss of correlation near the LF–HF transition [31]. This limitation is particularly relevant when simulated motions are used as inputs to portfolio risk, spatially distributed infrastructure assessment, or multi-period vector-valued engineering demand models.

The objective of this work is threefold. First, we develop and evaluate an enhanced version of the ANN architecture proposed by Paolucci et al. [13] to predict short-period spectral accelerations (SAs) from long-period SAs obtained from PBS. More broadly, ML methods have increasingly supported engineering seismology by improving ground-motion prediction, early-warning performance, earthquake catalogue development, and other data-driven seismic analyses [32]. Second, we use transfer learning (TL) [33] to adapt the proposed ML workflow to regions with scarce strong-motion recordings: an ANN is first pretrained on a large global ground-motion dataset to learn robust magnitude–distance scaling and other transferable trends, and is then fine-tuned using a limited local dataset. Recent applications of TL in earthquake engineering include rapid prediction of ground-motion intensity measures [34] and the development of ground-motion models for data-limited regions [35]. Third, we develop an empirical multivariate correlation model for the within-event residuals of the ANN predictions, enabling the generation of spatially, spectrally, and cross-component correlated broadband ground-motion fields relevant to hazard and risk applications. These fields can be generated unconditionally for scenario-earthquake applications, or conditionally on observed ground motions, for example when reconstructing historical earthquakes.

The paper is structured as follows. We first present the proposed ANN for estimating broadband response spectra from PBS results, and then we describe how the model can be regionally adapted when only limited local data is available. We then discuss the modelling of spatial and cross-period/cross-component correlation of within-event residuals that can be jointly used with the ANN predictions. Finally, the methodology is applied and evaluated using low-frequency PBS of South Iceland earthquakes [36], followed by a discussion of implications and limitations for engineering applications. Compared with recent hybrid broadband simulation approaches, the present work combines three-component ANN-based short-period spectral prediction, regional transfer learning, and a multivariate residual model for spatial, inter-period, and cross-component dependence.

2 ANN to predict short-period spectral ordinates

2.1 ANN2BB method

Paolucci et al. [13] proposed a hybrid data-driven simulation framework, termed artificial neural network to broadband (ANN2BB), to generate BB ground motions by extending physics-based LF simulations with data-driven predictions of short-period response spectra. The core idea is that, for a given LF simulated ground motion, short-period spectral accelerations $SA(T<T^*)$ can be inferred from the long-period ordinates $SA(T\geq T^*)$ computed from PBS. This mapping is performed using two-hidden-layer feed-forward ANNs, trained with records separately for the geometric mean of the horizontal components (GMH) and for the vertical component SA. The resulting target spectrum is obtained by concatenating the predicted short-period ordinates with the simulated long-period ordinates, i.e., $SA(T<T^*) \cup SA(T\geq T^*)$. High-frequency (HF) time histories are then generated using the non-stationary stochastic method of Sabetta et al. [37], and the scaled realization whose response spectrum best matches the target spectrum is selected. Finally, the selected HF signal and the

LF physics-based waveform, after applying complementary high- and low-pass filtering, respectively, are merged in the time domain to form a BB seismogram. The transition period T* (equivalently, the transition frequency) is chosen based on the maximum resolvable frequency of the physics-based simulation.

The ANN2BB methodology has been applied to a variety of earthquake scenarios spanning a broad range of magnitudes, faulting styles, and geological settings, which were compiled in the BB-SPEEDset database [38]. These BB simulations were shown to reproduce, in a statistical sense, peak values, integral intensity measures, durations, and attenuation trends consistent with recorded near-fault motions, as found from the NESS database [39]. Nevertheless, the original ANN2BB formulation exhibits some limitations that motivate the developments proposed in this study. First, the ANNs are trained using only long-period spectral accelerations as inputs. When residuals are examined as a function of Joyner–Boore distance (R_{JB}), this formulation can lead to systematic distance-dependent bias. This effect was not evident in [13] because residuals were analysed primarily as a function of period, for which no bias was observed. Second, for the horizontal components the ANN is trained on GMH, while the two horizontal components are subsequently generated independently. As a result, strong polarization present at long periods may be implicitly transferred into the predicted short-period ordinates, because the ANN acts purely as a mapping between spectral shapes without explicit control of cross-component behaviour. This is potentially problematic in the near field, where long-period ground motion is often strongly polarized due to rupture directivity and source radiation effects, but such polarization tends to diminish at higher frequencies, largely due to the combined influence of short-wavelength rupture heterogeneity and path scattering arising from small-scale velocity fluctuations [40,41]. These issues are addressed through an improved ANN architecture described in the following section.

2.2 Architecture of the ANN

Artificial neural networks are flexible, data-driven models designed to learn complex nonlinear relationships between input and output variables directly from examples [42,43]. Unlike closed-form empirical regressions, where functional forms and interaction terms must be specified a priori, ANNs can automatically capture coupled effects, nonlinearities, and variable interactions that are difficult to represent analytically, particularly when the mapping depends on many correlated predictors. From a functional perspective, feed-forward ANNs approximate the target relationship through a composition of affine transformations and nonlinear activation functions, and, under mild conditions, can approximate a broad class of continuous functions [44]. During training, network parameters are optimized to minimize a loss function that quantifies the mismatch between predicted and observed outputs, commonly using gradient-based algorithms [43], while techniques such as early stopping and dropout are often adopted to improve generalization [45]. This makes feed-forward ANNs suitable for broadband ground-motion prediction, where the relationship between components, and long-period and short-period spectral ordinates is strongly nonlinear and influenced by multiple coupled factors.

The proposed model is a multi-branch feed-forward ANN, equivalent to a multilayer perceptron (MLP), consisting of six input branches (Figure 1). The first three correspond to the as recorded long-period spectral accelerations of the two horizontal components and the vertical component. The fourth branch includes scalar source and path parameters. Finally, the last three branches include EC8 site class (SC: A, B, C, or D), faulting mechanism (FM: normal - NF, reverse/thrust - TF or strike-slip - SS), and region (RG: Italy - IT, California - CA, Taiwan - TW, Türkiye - TR, Japan – JP, or Other – OT), respectively. These three branches are represented by a one-hot encoded vector, that for instance, it would be [1,0,0,0] for SC A, [0,0,1] for strike-slip FM, and [0,0,0,1,0,0] for Türkiye.

Each input branch is first processed independently through a fully connected layer. Hyperbolic tangent (tanh) activation functions are used for the first four branches, while rectified linear unit (ReLU) activation functions are used for the categorical branches. The resulting branch outputs are merged through a concatenation layer, which is then passed to a shared fully connected hidden layer with a tanh activation function. Processing these input groups through separate branches allows the network to learn distinct representations for spectral shape, scalar source–path effects, and categorical metadata before combining them. This structure also provides a more transparent organization of the predictors thana single fully connected input layer.

The shared layer is connected to three separate output layers with linear activation functions, each predicting the short-period spectral accelerations of horizontal and vertical components. To ensure comparability across variables, z-score normalization is applied to the first four input branches. Input and output spectral accelerations are given in natural logarithmic scale ln(SA), with SA in m/s^2. For each component we use a total of 29 SAs for periods going from 0 to 5 sec. These 29 periods are divided into input/output depending on the transition period T*. For instance, for T*=1 s, the output periods are [0,0.05,0.07,(0.1:0.05:0.5),0.6,0.7, 0.75,0.8,0.9] s, while the remaining longer periods are used as spectral inputs.

The main architectural hyperparameters are the width of the branch-specific layers, N_1, and the width of the shared hidden layer, N_2 (see Figure 1). For the reference model, N_1 is set equal to the number of long-period input ordinates per component, and N_2 is set equal to three times the number of short-period output ordinates per component. These values were selected using the architecture-sensitivity analysis reported in the Supplemental Material. Overall, the reference architecture was retained as a parsimonious compromise between predictive accuracy, generalization, bias control, and model complexity.

With respect to the ANN proposed by [13], we augment the inputs with source, path, and site parameters commonly used in GMMs, as this has been shown to improve predictive performance in related ANNs [46]. A further and key distinction from existing ANN approaches for estimating spectral ordinates [13,14,46,47] is that we model the three components simultaneously. Because the long-period spectral ordinates are provided as inputs, the network is implicitly conditioned on event- and path-specific effects embedded in the LF motion, such as rupture directivity, distance-dependent attenuation, and source characteristics that control spectral shape, thereby enabling a more event-specific mapping than would be possible using a GMM with only scalar metadata. In this sense, the proposed ML model can be interpreted as a data-driven, non-parametric generalized ground-motion prediction model [48], summarized as

$$\ln \mathbf{SA}(\mathbf{T} < \mathbf{T}^{*})^{(\mathbf{H1,H2,V})} = \mathbf{f}_{\boldsymbol{\theta}}\left(\ln \mathbf{SA}(\mathbf{T} \geq \mathbf{T}^{*})^{(\mathbf{H1,H2,V})}, \mathrm{M_w}, \mathrm{R_{JB}}, \ln(\mathrm{R_{JB}}), \mathrm{D_h}, \mathrm{SC}, \mathrm{FM}, \mathrm{RG}\right), \tag{1}$$

where $\mathbf{SA}(\mathbf{T} < \mathbf{T}^{*})^{(\mathbf{H1,H2,V})}$ and $\mathbf{SA}(\mathbf{T} \geq \mathbf{T}^{*})^{(\mathbf{H1,H2,V})}$ denote the stacked short- and long-period spectral accelerations for the two horizontal components and the vertical component, and $\mathbf{f}_{\boldsymbol{\theta}}$ is the trained ANN.

By jointly learning the mapping for the two horizontal and vertical components, the ANN can model physically plausible cross-component dependence at short periods, while allowing to capture the ground motion polarization features at short periods, consistent with observed ground motion behaviour, which typically shows a decreasing trend as frequency increases

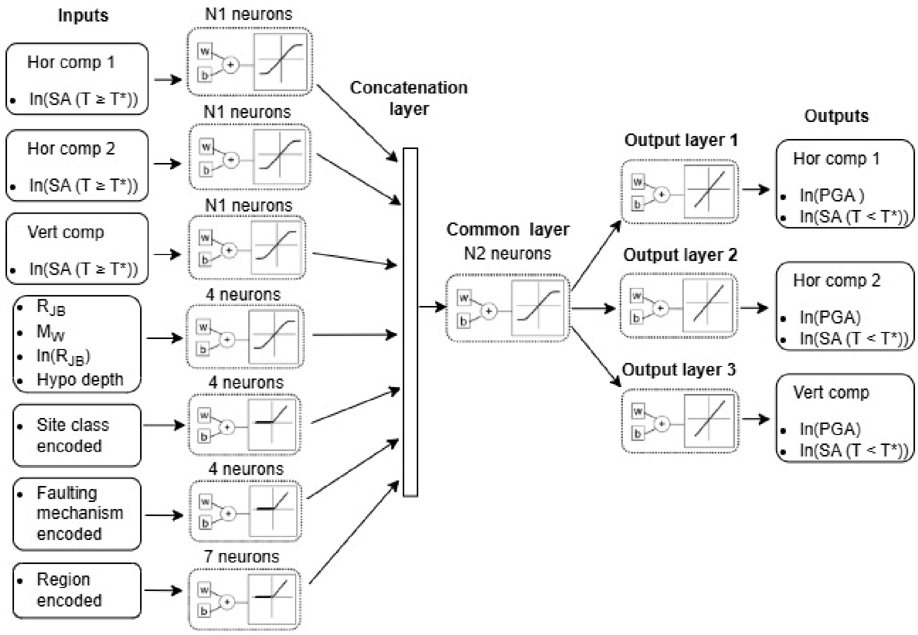

Figure 1. Architecture of the multi-branch feed-forward artificial neural network model to predict three-component short-period response spectra SA(T<T*) from long-period spectra SA(T≥T*), R_{JB} (Joyner-Boore distance), ln(R_{JB}), M_w, hypocentral depth (D_h), site class, faulting mechanism, and region.

2.3 Dataset and training

The training dataset combines records from earthquakes with $M_w \geq 5$ and $R_{JB} \leq 130$ km from the ESM database [49], together with records from earthquakes with $M_w \geq 6.5$ from the NGA-West2 database [50]. The combination of ESM and NGA-West2 data was adopted to ensure adequate coverage of both moderate-to-large magnitudes and near-fault distances, while maintaining sufficient diversity in tectonic setting, site conditions, and source characteristics to support robust ANN training. The combined dataset consists of a total of 5148 three-component strong-motion records from crustal earthquakes with hypocentral depths less than 30 km. Figure 2 shows the M_w vs R_{JB} distribution of the records used for training the model.

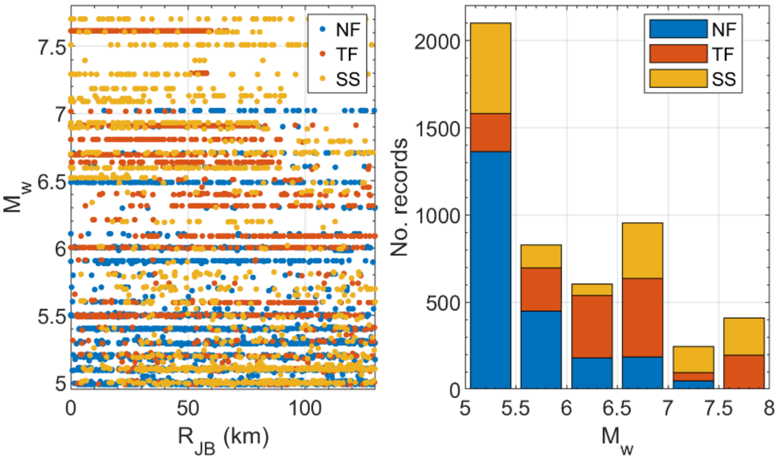

Figure 2. Magnitude M_w vs R_{JB} scatter plot of recordings in the ESM+NGA-West2 dataset used for training the ANN, including 5148 strong-motion records from crustal earthquakes (left). Points are color-coded by focal mechanism: NF (normal), TF (reverse/thrust), and SS (strike-slip). Histogram of the number of events per magnitude bin (right).

The network is trained using MATLAB's *trainnet* function [51] with Adam optimizer [52] and a composite loss function. For each output head, the misfit is measured using the Huber function [53] with threshold δ=1 (in natural-log units), which behaves quadratically for small residuals and linearly for large residuals. This choice provides robustness against outliers while retaining sensitivity to small residuals, which is desirable given the heterogeneous quality and recording conditions of strong-motion datasets. Residuals are computed for each period and averaged over the mini-batch, then aggregated across periods. To discourage systematic offsets, we add a bias penalty proportional to the squared mean residual per period, with increased emphasis on the short-period range where prediction uncertainty is largest and engineering sensitivity is highest. Moreover, to reduce the dominance of abundant low-magnitude and distant records during training, inspired by the recently proposed HazBinLoss [54], a record-level weight was introduced in the loss function, where larger weights are assigned to records that are more relevant for hazard assessment, particularly large-magnitude and near-source motions. This weight is defined as

$$w_i = \frac{1+\beta H_i}{\frac{1}{N_{\mathrm{tr}}}\sum_{j=1}^{N_{\mathrm{tr}}}(1+\beta H_j)}, with\ H_i = S_M(M_{w,i})\left[\gamma + (1-\gamma)S_R(R_{JB,i})\right],$$
$$S_M(M_{w,i}) = \frac{1}{1+\exp[-a_M(M_{w,i}-M_0)]}, S_R(R_{JB,i}) = \frac{1}{1+\exp[-a_R(R_0-R_{JB,i})]}, \quad (2)$$

where M_0=6, R_0=20 km, a_M=2.5, a_R=0.2, γ=0.3 and β=5.

Finally, the three component losses are combined with larger weights for the two horizontal components , reflecting their primary importance in most engineering applications. The total loss is then

$$\mathcal{L}_{\mathrm{total}} = 0.375\mathcal{L}_{H1} + 0.375\mathcal{L}_{H2} + 0.25\mathcal{L}_{V}. \quad (3)$$

The initial learning rate was set to $5\cdot10^{-4}$ and it was reducing by half every 40 epochs. To prevent overfitting, early stopping was employed during training. The training data were split into three subsets using a record-wise partitioning: (1) a training set (72%), used to calibrate the adjustable ANN weights; (2) a validation set (18%), used to check the validation loss during training and stop the training if the validation loss did not improve for 6 consecutive epochs; and (3) a test set (10%), not used during ANN training and validation, but needed to evaluate the network capability of generalization in the presence of new data.

Figure S1 in the Supplemental Material illustrates learning curves of ANNs trained using as transition periods 0.7 s and 1 s. T*=1 s was chosen for many of the demonstrations since it is the transition period used for the Iceland case study in Section 6. The learning curves for both training and validation show a rapid decrease in the composite loss function during the initial epochs, followed by a gradual flattening as the model converges. This suggests that the model rapidly reaches an error floor that is primarily controlled by the information content of the available predictors, rather than by network capacity. In other words, once the principal trends captured by the input variables are learned, the remaining variability in the targets is largely attributable to effects not represented in the feature set (e.g., unmodeled source, path, and site complexity) and to irreducible record-to-record scatter. Under these conditions, increasing the number of neurons or adding additional layers yields only marginal reductions in training and validation loss, resulting in learning curves with limited further improvement after the initial epochs. Moreover, the training and validation losses remain very close throughout, indicating good generalization and no evident overfitting. The selected model corresponds to the epoch with the lowest validation loss.

Additionally, Figure 3 illustrates total residual bars corresponding to ±1 standard deviation (σ) from the predictions of the same ANNs for one horizontal component. Results are presented and compared for the training, validation, and test sets. No bias with period is observed in both cases. Uncertainties clearly increase at shorter periods, i.e., farther from T*. Despite this effect, the prediction accuracy for PGA is generally higher than for short periods. It is worth noting that in both cases, the total σ in ln-units of both the validation and test sets is bounded to ±0.7, which lies at the lower bound of typical total standard deviations reported by recent GMMs [55]. This comparatively low dispersion is likely attributable, at least in part, to including long-period SA among the predictors, which adds further constraints and reduces unexplained variability relative to conventional GMMs.

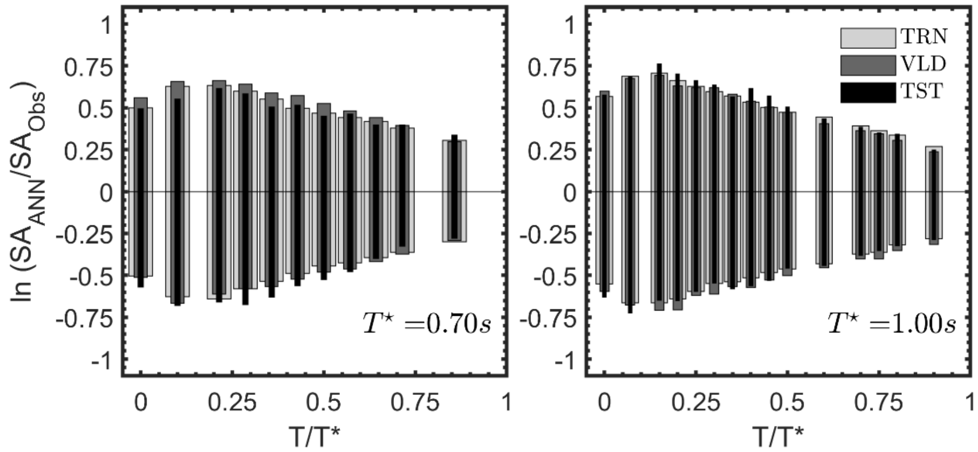

Figure 3. Performance of ANNs trained in predicting SA(T<T*) of the ESM+NGA-West2 data sets, expressed in terms of total logarithmic residuals for one horizontal component, i.e., ln(SA_{ANN}/SA_{Obs}), in which SA_{ANN} denotes the SA predicted by the ANN and SA_{Obs} are the observed ones. The performance is estimated at each vibration period T, here normalized with respect to the transition period T*. The error bars refer to the training (TRN), validation (VLD), and test (TST) sets.

For the ANN with T*=1 s, the performance metrics in Table S1 indicate good generalization (similar RMSE across training/validation/test) and a strong agreement between predicted and observed short-period spectral ordinates, with most errors within a factor of approximately $e^{0.42} \approx 1.5$ on average.

Incorporating additional predictor variables commonly used in NGA-West2–based GMMs [19], such as Z_{TOR}, Z_1, and fault dip, could further enhance the model's predictive performance and potentially reduce aleatory variability. These predictors were not included here because they are not available in the ESM database.

2.4 Model interpretability and evaluation of physical trends

Because neural-network models are not fully transparent and are often regarded as "black boxes" [54], we performed three diagnostic analyses to assess the physical consistency and traceability of the ANN predictions. First, we computed grouped permutation feature importance following the model-agnostic grouped permutation principle of [56]. The predictor groups were defined as the ANN input branches. For each predictor group g, the validation RMSE was first computed using the original inputs, $RMSE_0(T)$. The group g was then randomly permuted across records while all other input groups were kept unchanged, and the RMSE was recomputed as $RMSE_g(T)$. The absolute grouped permutation importance was defined as $I_g(T) = RMSE_g(T) - RMSE_0(T)$. The corresponding change in prediction error was used as a measure of the incremental influence, or model reliance, associated with each predictor group. Second, we evaluate the sensitivity of the predictions for one component to individual LF input ordinates of the same component. Third, we evaluated the model response within the training domain, including near-source and far-source scenarios, lower and upper magnitude ranges, and different site and region classes. These checks are not intended to provide a complete explanation of the network weights, but they help verify that the model response is controlled by physically meaningful inputs and does not exhibit obvious nonphysical trends.

Figure 4 shows the grouped permutation-importance (GPI) for the model with T*=1 s. To facilitate comparison among groups, we report the normalized contribution. Therefore, values in Figure 4 represent the percentage contribution of each predictor group to the total RMSE increase at a given output period. The results indicate that the ANN predictions are primarily controlled by physically meaningful input groups. At the shortest periods, the magnitude–distance–depth branch provides the largest contribution, reflecting the importance of source–path scaling where the target ordinates are farthest from the transition period. Toward T^*, the long-period spectral ordinates become dominant, especially for the corresponding component, confirming that the ANN mainly acts as a conditional spectral-continuation model. The figure also shows non-negligible cross-component dependence, as the long-period spectra of the other components contribute to the prediction, although less strongly than the corresponding component. This behaviour is expected for a jointly trained three-component model, because the different components share event-, path-, and site-specific spectral characteristics. Site class and faulting mechanism have much smaller incremental importance compared to the other branches, although perturbing these branches produces non-zero prediction changes. This suggests that the network uses these categorical predictors mainly as secondary corrections once the long-period spectral shape and source–path predictors are specified. Their limited permutation importance is consistent with the fact that the long-period spectral inputs already contain part of the source, path, and site effects that would otherwise need to be represented by categorical metadata.

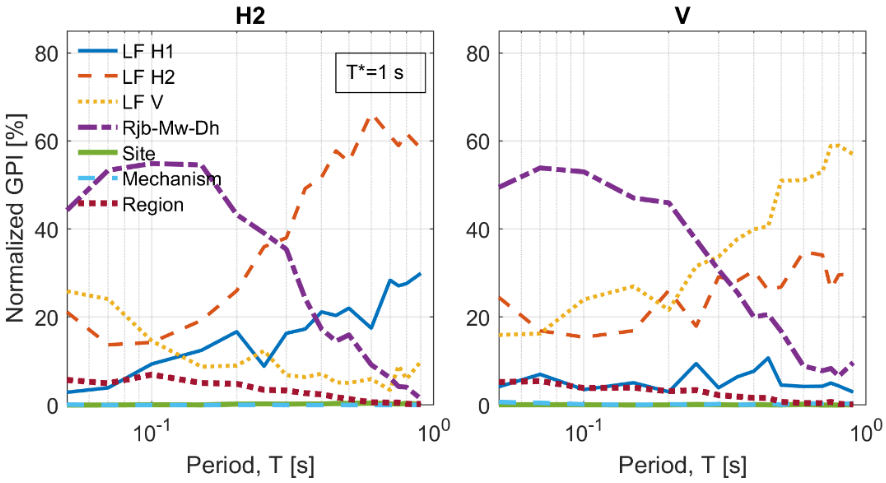

Figure 4 Grouped permutation importance (GPI) expressed as the percentage contribution of each predictor branch to the total RMSE increase at each output period, for the ANN with T*=1 s. Importance was computed on the validation set by jointly permuting each predictor group and averaging over 50 random permutations. H1 and H2 stand for the horizontal components 1 and 2, while V stands for the vertical component.

As an additional diagnostic, we evaluated the input-period perturbation sensitivity of one horizontal component to long-period input ordinates. For each selected long-period ordinate, an additive Gaussian perturbation in natural-log units was imposed and propagated to the remaining long-period ordinates according to the Baker and Jayaram inter-period correlation model [21]. For each perturbed input period, the RMS change in the predicted short-period spectrum of the same component was computed over the validation set and averaged over repeated perturbations. The sensitivities were then normalized at each output period so that the contributions of all perturbed input periods sum to 100%. Figure S2 shows that the largest sensitivity is associated with input periods close to the transition period, with maximum contributions of about 12–15%. The sensitivity gradually decreases toward longer input periods, indicating that the ANN mainly relies on the long-period spectral level and local spectral shape near the transition period to constrain the short-period continuation. Longer-period ordinates still contribute, but their influence is weaker and more diffuse, suggesting that they provide secondary information on the broader low-frequency spectral trend.

We then verified whether the ANN model reproduces key physical ground-motion trends, including attenuation with increasing R_{JB}, and magnitude/near-field saturation. SA estimates are obtained from the model with T*=0.7 s, with long-period input spectra computed from the GMM of Lanzano et al. [55] for the horizontal components, and Ramadan et al. [57] for the vertical one, according to the corresponding fault mechanism, M_w and R_{JB}. This setup allows the physical plausibility of the ANN mapping itself to be examined independently of physics-based simulation variability, by conditioning the model on smooth, well-established median trends. For forward applications and the results that follow, we use ensemble prediction [58] by training five models with different random split in training/validation/test sets, and averaging their outputs; this reduces prediction variance because idiosyncratic period-to-period fluctuations are not consistent across the ensemble models. Figure 5 compares estimated horizontal response spectra from the GMM by Lanzano et al. [55] and from the ANN, for various combinations of M_w and R_{JB}, considering normal faulting, EC8 site class is A, and Italy as region. The spectra show smooth behaviour across the transition period, with spectral peak shifting systematically to longer periods as M_w increases. Moreover, the agreement is good for magnitudes between 5 and 6.5, while some differences occur at periods around 0.2 s for M_w=7. On the other hand, Figure S3 shows regional differences and the effect of site class. Notably, the ANN estimates for the Taiwan (TW) region are systematically lower than those for other regions, a behaviour that has been consistently observed in empirical studies and is commonly attributed to stronger near-surface attenuation of high frequencies [59].

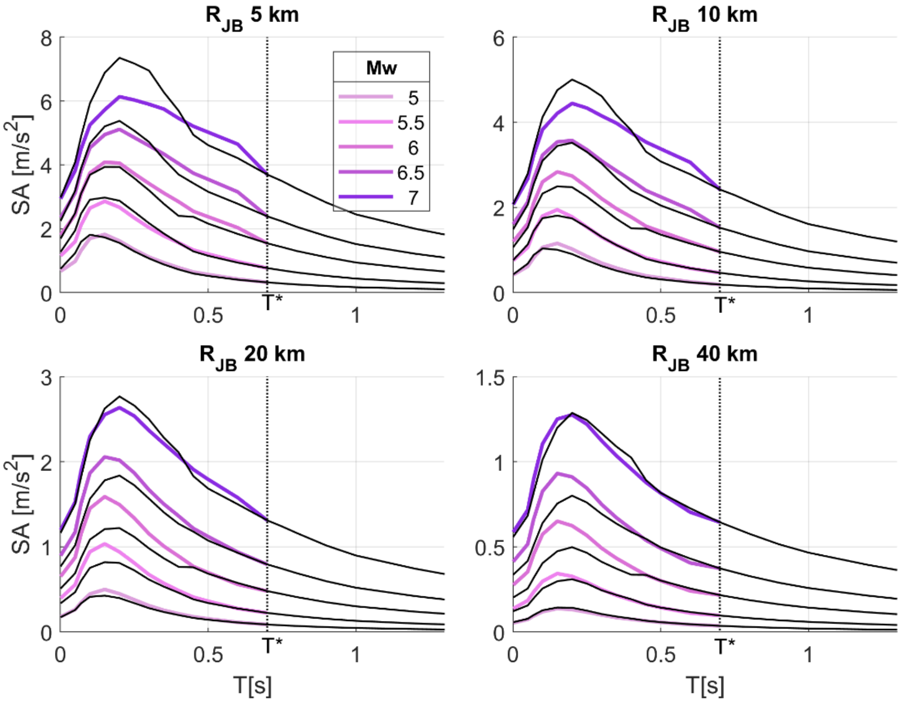

Figure 5. Comparison between estimated horizontal SA from the GMM by Lanzano et al. [55] (black lines), and from the ANNs with T*=0.7 s, for different combinations of M_w and R_{JB}, considering normal faulting, EC8 site class A, and Italy as region.

Figure 6 shows magnitude and distance scaling for PGA and SA(0.5 s), indicating limited increases beyond about M_w 7 and clear saturation at short distances. The saturation shifts towards larger distances as magnitude increases, reflecting near-field ground-motion saturation, empirically observed in ground motion models. Overall, these results indicate that the ANN reproduces the main physical trends of ground-motion propagation that are relevant for engineering applications, without introducing evident artefacts or non-physical scaling.

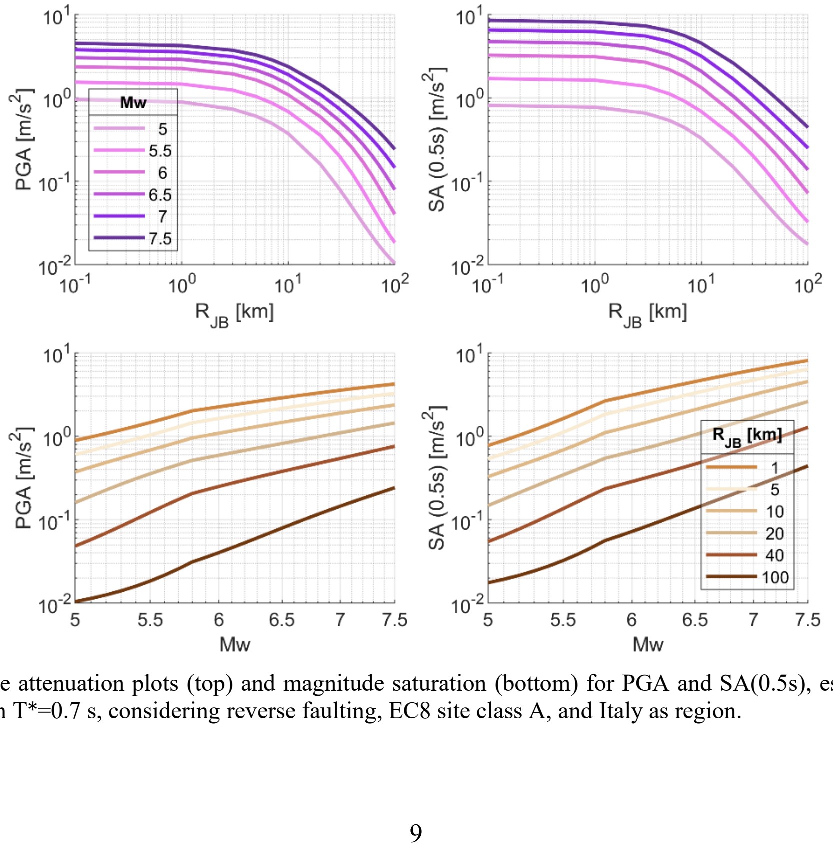

Figure 6. Distance attenuation plots (top) and magnitude saturation (bottom) for PGA and SA(0.5s), estimated from the ANN models with T*=0.7 s, considering reverse faulting, EC8 site class A, and Italy as region.

2.5 Analysis of residuals

Following standard ground-motion decomposition [60], a logarithmic intensity measure (here SA) for event e at site s and period T may be expressed as

$$\ln SA_{es}(T) = \ln \mu_{es}(T) + \delta B_e(T) + \delta W_{es}(T), \tag{4}$$

where $\ln \mu_{es}(T)$ is the median model prediction (here provided by the ANN), $\delta B_e(T)$ is an event term, and $\delta W_{es}(T)$ is the within-event residual. The event terms and within-event residuals are assumed to be uncorrelated and normally distributed with zero mean and standard deviations τ and ϕ, respectively.

We performed a mixed-effects regression on the total residuals separately for each period and component, from which we observed that the within-event standard deviation ϕ decreases systematically with increasing magnitude (see Figure 7), hence, the final mixed-effects regression was performed using a heteroscedastic model for ϕ, defined as

$$\phi(M_w)\begin{cases}\phi_1, & M_w \leq 5,\\ \phi_1 + (M_w - 5)\cdot(\phi_2 - \phi_1), & 5 < M_w < 6,\\ \phi_2, & M_w \geq 6.\end{cases} \tag{5}$$

Within-event standard deviations ϕ_1 and ϕ_2 for all output periods are shown in Figure S4 for the model with T*=1, for one horizontal component and for the vertical component. They vary approximately from 0.3 at periods close to T* and 0.7 at short periods, which is a trend similar to that observed in Figure 3 for the total residuals.

In order to evaluate the validity of our model, we plotted the between-event and within-event residuals against the predictor variables included in the model. Upper panel of Figure 7 shows within-event residuals of one horizontal component at various periods vs R_{JB}, while the lower panel shows their variation with respect to M_w. Figures S6 to S9 show comparisons against other predictor variables. In general, no bias is observed.

Interestingly, the between-event standard deviation τ estimated from the ANN residuals becomes very small and, for several longer periods, effectively vanishes (Figure S5). This occurs because the long-period spectral ordinates provided as inputs capture much of the systematic variability typically attributed to source and path effects (e.g., stress drop, directivity, and attenuation), leaving little coherent event-to-event offset in the residuals once the ANN prediction is removed. At longer periods this conditioning is even more effective, since long-period response is dominated by the coherent, low-frequency source–path content that is well represented by the input spectra; as a result, likelihood-based mixed-effects fits provide no support for an event random effect and the corresponding variance component collapses to the boundary, $\hat{\tau}(T) \approx 0$. Consequently, the remaining unexplained variability at those periods is primarily within-event. This behaviour should not be interpreted as an absence of event-to-event variability in ground motion; rather, it indicates that, conditional on the input spectra, there is little additional event-level structure left to be captured by τ.

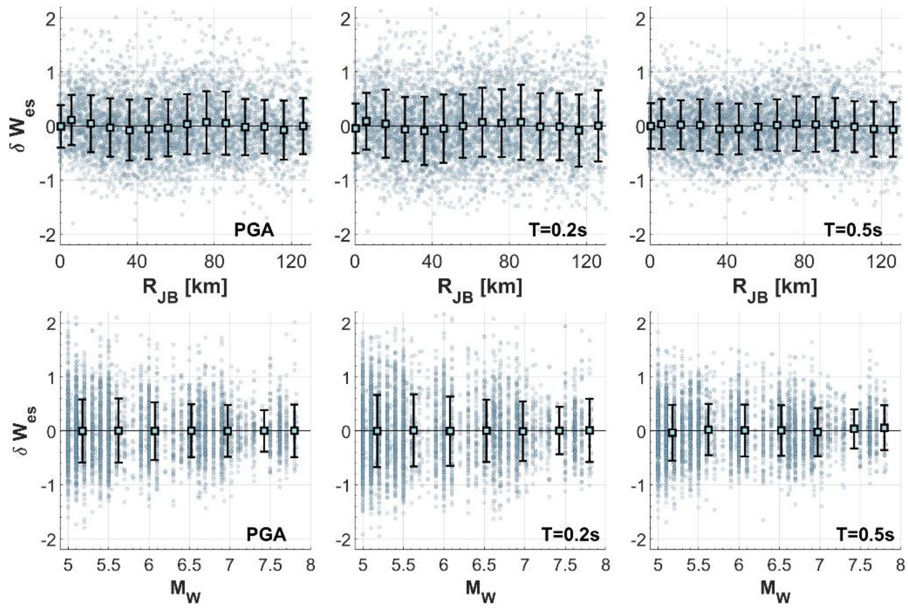

Figure 7. Within-event residuals for a horizontal component at different periods T vs R_{JB} (top panel) and vs M_w (lower panel). Error bars indicate ±1 standard deviation at various bins. T*=1 s.

3 Transfer learning

Although the ANN model presented in the previous section incorporates a degree of non-ergodicity by including a dedicated input branch with one-hot encoded region indicators, it is still trained as a single shared model across multiple regions and therefore cannot fully capture region-specific attenuation and near-source scaling characteristics. Because ML models are data-intensive, training a robust ANN using only a limited regional dataset is often impractical and would likely lead to overfitting. This is illustrated in Figure S10, which shows the residuals for the training, validation and tests subsets of two models trained with the Icelandic strong-motion dataset IceSMN [61], comprising only 90 tectonic strong-motion records. Although the training residuals are comparatively smaller and mostly centred around zero, the validation and test residuals exhibit large, period-dependent deviations, with overprediction at some periods and underprediction at others. Moreover, the residual patterns differ between the two models, indicating that the fitted response is sensitive to the particular data split and model configuration rather than representing a stable period-dependent regional correction. This behavior is consistent with overfitting caused by the limited size and coverage of the local dataset, which does not adequately constrain the mapping between long-period spectral ordinates, source/path/site predictors, and short-period response. In addition, because the maximum magnitude represented in the local dataset is $M_w 6.5$, a model trained exclusively on these data would require unconstrained extrapolation when applied to larger-magnitude scenarios. Such extrapolation would be unreliable, particularly for engineering applications where larger events may control the hazard and where the near-source and magnitude-scaling behavior must remain physically plausible. Consequently, training an ANN exclusively on the local dataset was not adopted.

To address this limitation, we adopt transfer learning (TL) [33], in which a model pretrained on a larger "source" dataset is adapted to a smaller "target" dataset. This use of TL does not assume full geophysical stationarity between the source and the local dataset. Rather, the pretrained model is used to learn broadly transferable magnitude–distance–site trends and the mapping between long- and short-period spectral ordinates, while the fine-tuning stage adjusts this mapping to the regional characteristics of the Icelandic data. In the implementation used here, the early (input and initial hidden) layers are frozen, whereas the shared and output layers are fine-tuned using regional data. This retains the more general features learned from the source dataset, whereas updating the final layers allow regional adjustment while limiting overfitting through early stopping.

The decision to update the shared and output layers during the fine-tuning was based on a simple ablation test. Two fine-tuning configurations were compared. In Case A, corresponding to the reference configuration adopted in this study, both the shared hidden layer and the output layers were updated. In Case B, only the output layers were updated, while the shared layers were kept frozen. Each configuration was trained five times using different random partitions, and the average validation and test RMSE and bias were computed. The results, shown in Figure S11, indicate that the reference configuration consistently provides lower RMSE and lower absolute bias than the output-only configuration. This suggests that updating only the final output layers is too restrictive for the target-region calibration, because it allows only a limited adjustment of the mapping learned from the global dataset. Allowing the shared layer to be updated provides additional flexibility to adapt the intermediate spectral representation to the regional data, while still retaining the general low- to high-frequency mapping learned during pretraining. Therefore, the configuration in which both shared and output layers are fine-tuned, was adopted in the final model.

3.1 Application of TL for Iceland

We applied the TL technique to fine-tune the previously developed ANN with T*=1 s, using the IceSMN dataset. The introduction of TL was motivated by well-documented regional differences in attenuation and near-source scaling in Iceland, whereby commonly used GMMs tend to underpredict short-distance motions and overpredict motions at larger distances [62,63]. The same distance-dependent bias was observed in the residuals obtained when the global ANN was applied to IceSMN (not shown here for brevity), indicating the need for region-specific calibration through fine-tuning.

The surface geology of the South Iceland Lowland results from a combination of volcanic activity, glacial drift, and changes in sea level through the ages. In many areas, sedimentary layers have been covered by layers of basaltic lava and hyaloclastite breccia from the post-glacial period, thus creating soil structures with thin layers of lava rock on top of, or embedded in, unconsolidated sediments [64,65]. This complex near-surface geology makes Vs_{30}, and hence EC8 site classes based on Vs_{30}, not good predictors of the site response for the unique site conditions in Iceland. Therefore, we decided not to use EC8 site classes as input, as previously done for the global ANN. Based on the work of Darzi et al. [66], we defined four geology-based categories (Figure S10), roughly representing hard rock, soft rock, lava with interbeds and thick soil deposits. These were developed by cross-referencing geological maps with site-to-site residuals (δS22) from the IceSMN dataset with respect to a local GMM. These geology-based categories are given as input in the same way as EC8 site classes, i.e., in encoded form.

It should be noted that while we use site classes as a predictor for site-effects, mostly due to the need for the Iceland case, however, Vs_{30} could be used instead as a predictor variable in the fourth branch of the ANN.

Because the TL stage, in this case, relies on a very limited regional dataset, naïve fine tuning can lead to high-variance updates that overfit period-specific noise rather than physically meaningful spectral trends. With relatively few examples per period, the loss can be reduced by fitting idiosyncratic, sample-specific fluctuations at individual periods rather than learning a smooth spectral shape, which manifests as jagged response spectra with spurious local peaks. To mitigate this effect, we introduce two complementary variance-reduction strategies. First, we apply an L^2-SP regularization term that penalizes deviations of the updated parameters from the pretrained weights [67], thereby anchoring the fine-tuning to physically plausible trends learned from the larger source dataset while allowing only modest regional adjustments. Second, we add a curvature (roughness) penalty on the predicted spectra, implemented via a squared second-difference term across adjacent periods, which directly discourages rapid oscillations in $\ln SA(T)$ and promotes smooth spectral shapes consistent with GMMs. Together, these measures improve the stability of the fine-tuned spectra without materially altering the underlying mean trends. Figure 8 presents the within-event residuals as a function of R_{JB} for the transfer-learned ANNs (T*=1 s) after fine-tuning on the Icelandic dataset. No systematic distance dependence is evident, indicating that the distance-related bias observed prior to fine-tuning has been effectively mitigated.

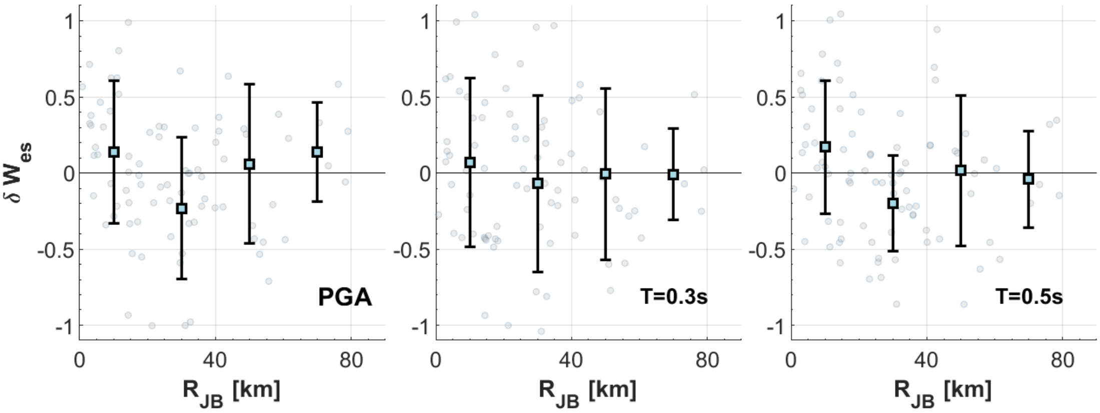

Figure 8. Within-event residuals for a horizontal component at different periods T vs RJB. Residuals are computed with respect to the average ensemble prediction of 5 ANNs with T*=1 s trained using TL with the Icelandic IceSMN dataset.

4 Spatial and inter-period correlation modelling of within-event residuals

For many earthquake-engineering applications, it is not sufficient to reproduce only the marginal distribution of response spectral ordinates at a site (i.e., median and standard deviation at each period). Scenario-based shaking maps, spatially distributed infrastructure assessments, and portfolio loss calculations are sensitive to the joint behaviour of ground motions across (i) space, (ii) period (or frequency), and often (iii) component. Empirical evidence from recordings shows that within a given event, spectral accelerations at nearby sites tend to deviate from the median in a coherent manner (spatial correlation), and that deviations at different periods are not independent (inter-period correlation). These dependencies can materially affect computed risk metrics, and neglecting them can bias loss and safety estimates [22,25–27].

In this work, correlation modelling focuses on within-event residuals, because they govern the event-specific spatial variability around a median prediction and therefore directly control the spatial coherence of simulated intensity-measure fields. Moreover, as shown earlier, between-event residuals are strongly reduced due the inclusion of long-period spectra as predictor variables. Following Loth and Baker [18] (hereafter LB13), we used normalized within-event residuals obtained from Eq. 4 as

$$\varepsilon(T) = \frac{\delta W_{es}(T)}{\phi(T)} = \frac{\ln SA_{es}(T) - \ln \mu_{es}(T) - \delta B_e(T)}{\phi(T)}. \tag{6}$$

Normalization by the heteroscedastic within-event standard deviation ensures that residuals at different periods and components are placed on a comparable scale prior to correlation modelling. With respect to previous works that focused only on within-event residuals of horizontal (invariant, e.g., RotD50) measures of SA or Fourier spectra [18,24,68], we aim to build a model for the joint dependence of $\varepsilon(T < T *)$ over periods, space and components.

4.1 Geostatistical formulation: covariance and semivariograms

A convenient and widely used geostatistical description of spatial dependence is the cross-semivariogram. For a multivariate residual vector field $\boldsymbol{\varepsilon}(s)$, under assumptions of second-order stationarity and isotropy (dependence only on separation distance h) over the spatial domain considered for a given even, the semivariogram matrix function is defined as

$$\boldsymbol{\Gamma}(h) = \frac{1}{2}\,\mathbb{E}[(\boldsymbol{\varepsilon}(s) - \boldsymbol{\varepsilon}(s+h))(\boldsymbol{\varepsilon}(s) - \boldsymbol{\varepsilon}(s+h))^{\mathsf{T}}], \tag{7}$$

where s represents spatial position. The corresponding covariance matrix function $\mathbf{C}(h)$ satisfies

$$\mathbf{C}(h) = \mathbf{C}(0) - \boldsymbol{\Gamma}(h), \tag{8}$$

so that $\mathbf{C}(0)$ is the co-located covariance across variables (periods and components), while $\mathbf{C}(h)$ for $h > 0$ controls cross-site dependence.

A crucial requirement of any multivariate spatial correlation model is admissibility: for any set of locations $s_1, \ldots, s_N$, the full covariance matrix formed by $\mathbf{C}(h_{ij})$ must be positive semidefinite. This requirement is essential for both unconditional simulation and conditional simulation (kriging/conditioning). LB18 emphasize that fitting each period-pair semivariogram independently can lead to covariance matrices that are not positive definite, motivating the use of structured multivariate models that guarantee admissibility by construction. A simple and computationally attractive assumption is separability of $\mathbf{C}(h)$ into a single scalar correlation function $\rho(h)$ governing spatial decay, and a matrix $\mathbf{C}(0)$ capturing inter-period covariance at one site. Separable models guarantee admissibility if $\rho(h)$ is a valid correlation function and $\mathbf{C}(0)$ is positive semidefinite, but they can be overly restrictive. Empirical semivariograms often indicate multiple spatial scales (e.g., a rapid initial increase at small h plus a slower approach to the sill), and the effective range can vary with period. LB18 show that a single-range separable form may not reproduce observed behaviour across all period pairs, and propose nested multiscale models as a practical remedy.

4.2 Linear Model of Coregionalization (LMC)

A standard and flexible multivariate geostatistical model is the Linear Model of Coregionalization (LMC), in which the semivariogram matrix is expressed as a sum of a small number of admissible scalar structures g_ℓ, multiplied by coregionalization matrices $\mathbf{P}^\ell$. The LMC is attractive because admissibility of the resulting covariance is ensured if all coregionalization matrices are positive semidefinite. For ground-motion residuals, both LB13 and Wang et al. [24] (hereafter WO21) adopt a nested model with two exponential functions $g_\ell(h) = 1 - \exp(-3h/R)$, plus a nugget. R is known as the correlation length. Using the covariance representation (often more convenient for simulation), a two-range + nugget LMC can be written as

$$\mathbf{C}(h) = \mathbf{P}^1 \exp\left(-\frac{3h}{R_1}\right) + \mathbf{P}^2 \exp\left(-\frac{3h}{R_2}\right) + \mathbf{P}^3\, \mathbb{I}_{\{h=0\}}, \tag{9}$$

where $\mathbf{P}^1$ and $\mathbf{P}^2$ are short- and long-range coregionalization matrices, $\mathbf{P}^3$ is a nugget matrix, and $\mathbb{I}_{\{h=0\}}$ is an indicator function equal to 1 for co-located values and 0 otherwise. R_1 and R_2 are the short- and long-range correlations lengths, respectively. The nugget term produces a discontinuity between $h = 0$ and $h \to 0$, representing micro-scale variability and/or site-specific effects that are not spatially shared between distinct locations. Importantly, the model implies that the co-located covariance is

$$\mathbf{C}(0) = \mathbf{P}^1 + \mathbf{P}^2 + \mathbf{P}^3, \tag{10}$$

which simultaneously defines the inter-period covariance at a single site and, together with the range terms, the cross-site covariance for $h > 0$. This dual role of $h = 0$ and $h > 0$ is emphasized by WO21 and is equally present in the nested LMC used by LB13.

4.3 Empirical estimation and fitting of nested LMC models

The empirical semivariogram matrix is typically computed by binning pairwise differences of within-event residuals by separation distance. Because the aim is to model within-event spatial variability, pairs are formed only from records belonging to the same earthquake, thereby avoiding contamination from between-event effects. LB13 and WO21 both adopt this within-event pairing principle. Denoting by $\Delta\boldsymbol{\varepsilon}_{ij} = \boldsymbol{\varepsilon}(s_i) - \boldsymbol{\varepsilon}(s_j)$ the residual difference vector for a pair of sites with separation h_{ij}, the empirical semivariogram matrix in a distance bin k is

$$\hat{\boldsymbol{\Gamma}}(h_k) = \frac{1}{2n_k} \sum_{(i,j)\in k} \Delta\, \boldsymbol{\varepsilon}_{ij}\, \Delta\boldsymbol{\varepsilon}_{ij}^{\mathrm{T}}, \tag{11}$$

where n_k is the number of pairs in bin k.

To estimate $\mathbf{P}^1$, $\mathbf{P}^2$, $\mathbf{P}^3$ for prescribed ranges R_1, R_2, LB13 use a variant of the Goulard–Voltz [69] iterative algorithm. In essence, for fixed basis functions $g_\ell(h_k)$, the matrices $\mathbf{P}^\ell$are updated by weighted least squares so that the model semivariogram best matches $\hat{\boldsymbol{\Gamma}}(h_k)$ across bins. Weighting is used to stabilize the fit, placing greater emphasis on shorter distances (weights proportional to $1/h_k$). WO21 similarly uses weighted fitting and then enforces positive semidefiniteness through eigenvalue truncation after each update. These steps help ensure the resulting covariance is admissible for simulation.

Because the diagonal of an empirical semivariogram at large distances may not perfectly reach its theoretical sill due to finite sample effects and uneven station geometry, coregionalization matrices can be normalized such that the diagonal terms of $\mathbf{C}(0)$ are equal to one, to maintain consistency with the intended variance and correlation interpretation [18]. Hence, the resulting $\mathbf{C}(0)$ is a correlation coefficient model.

4.4 Extension to short-period SAs and three-components

The nested LMC framework is naturally extensible to simultaneously represent inter-period and inter-component dependence. In this work, we model SA(T<T*) for three components simultaneously, hence we stack residuals into a single multivariate field as

$$\boldsymbol{\varepsilon}(s) = [\varepsilon_{H1}(s,T_1), \dots, \varepsilon_{H1}(s,T_{n_P}), \varepsilon_{H2}(s,T_1), \dots, \varepsilon_{H2}(s,T_{n_P}), \varepsilon_v(s,T_1), \dots, \varepsilon_v(s,T_{n_P})]^{\mathrm{T}}, \tag{12}$$

so that $p = 3n_P$ (e.g., n_P=17 for the ANN with T*=1 s). In this form, $\mathbf{C}(0)$ encodes (i) inter-period correlations within a component, (ii) cross-component correlations at the same period, and (iii) cross-component/cross-period correlations, while the spatial ranges R_1, R_2 control how quickly these dependencies decay with distance. This is aligned with the modelling philosophy of LB13, but here it is tailored to the short-period SA range and to multi-component ANN-based broadband prediction.

The two-range + nugget model of Eq. 9 is fitted with $\mathbf{P}^\ell \in \mathbb{R}^{p\times p}$, using the Goulard–Voltz algorithm, with the normalization and weights mentioned in the previous section and used by WO21. In fitting the LMC model we use only residuals from events with more than 12 records, hence, only 3566 from the 5148 records in Figure 2 were used, corresponding to 57 events. Moreover, when fitting the model we do not differentiate by M_w, site or regional classes, since it has been previously shown that although there might be important event-to-event variability in spatial correlation, there is little statistically significant dependence of the spatial [24,70] and inter-period [20,71] correlation on these variables, especially at short periods. We searched iteratively for the optimum (minimum weighted sum of squares - WSS) pair R_1, R_2 in a range close to the values used by WO21 of 10 km 100 km, respectively. For the ANN with T*=1 s, R_1=6 km and R_2=95 km. Figure 9 compares the empirical semivariogram matrix with the fitted nested LMC model for some representative periods for the horizontal component 1 (H1). The same comparison is presented in Figure S10 for the vertical component. These figures demonstrate that the two-range structure captures both the near-field correlation and the decay with separation distance.

Figure 10 shows the co-located covariance matrix C(0). Periods in each block increase from left to right and from top to bottom. First of all, we observe that the diagonal blocks, which represent the inter-period correlations, are very similar for both horizontal components. This was expected since they are as-recorded components and are not aligned to any specific direction with respect to the source. Clearly, if they were aligned to the principal directions [72] or to fault-normal and fault-parallel directions, a different pattern might have been observed. Moreover, we observe that the cross-component correlation between horizontal components is larger than between horizontal and vertical components. For instance, the correlation coefficient between PGA_{H1} and PGA_{H2} is 0.85, while between PGA_{H1} and PGA_V it is 0.73. Finally, the inter-period correlation of horizontal components is slightly larger than for the vertical component.

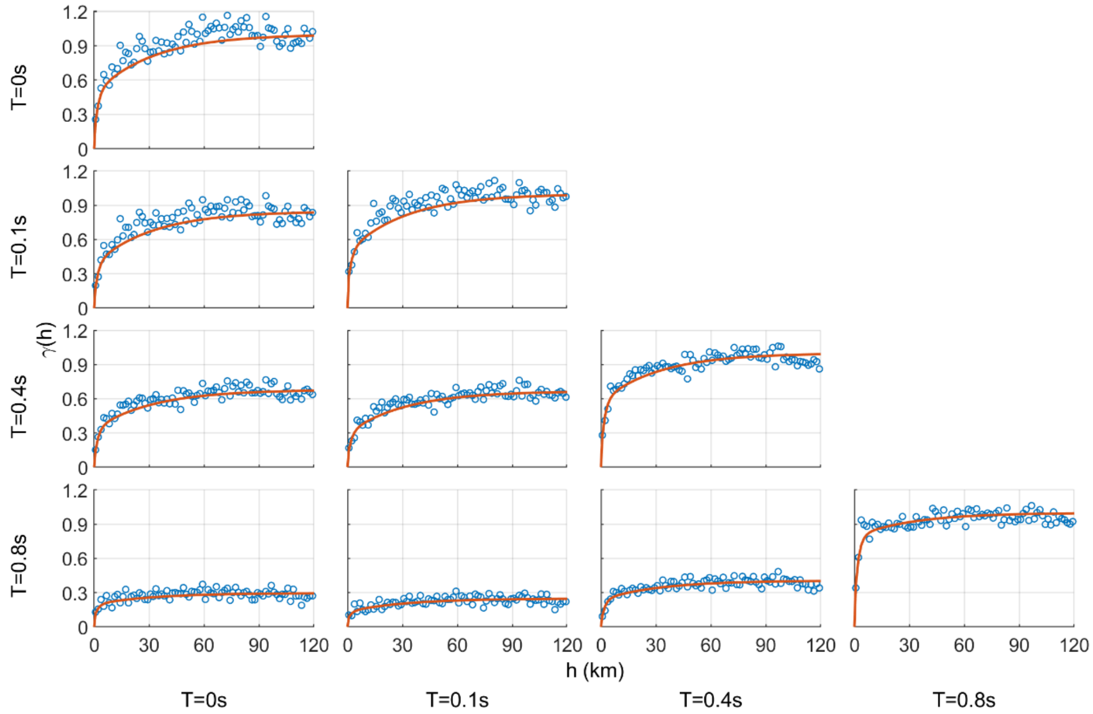

Figure 9. Empirical semivariograms of within-event residuals and the fitted multivariate semivariogram model (solid lines) for horizontal component H1 at period pairs for 0.0, 0.1, 0.4 and 0.7 s. Residuals are computed with respect to the predictions by five ANNs with T*=1 s.

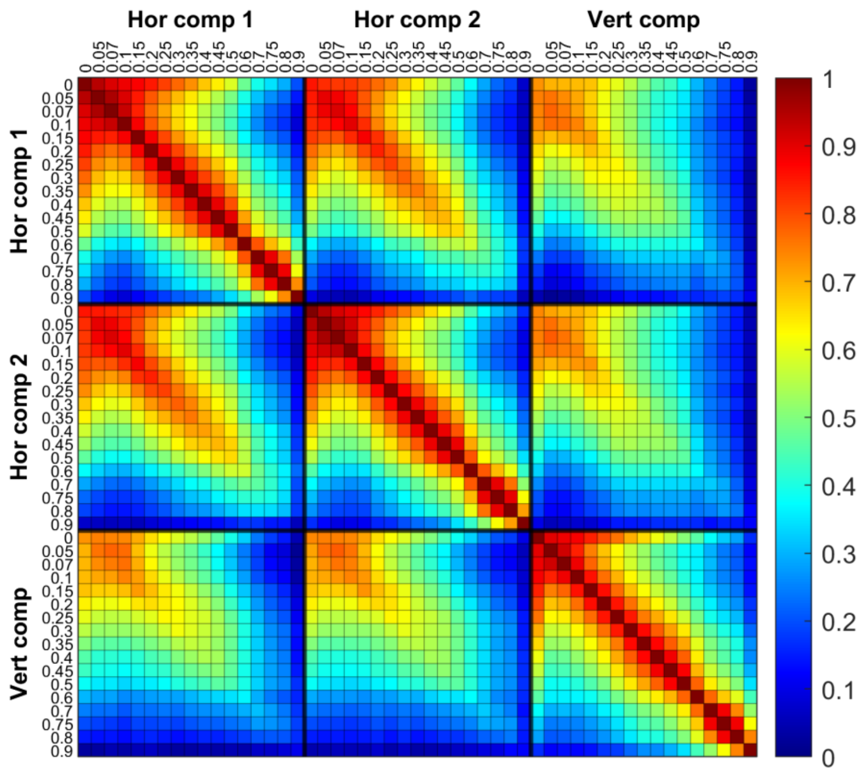

Figure 10. Co-located covariance matrix C(0) in graphical form, showing the correlation coefficients between periods, components, and component–period pairs. Periods in each block increase from left to right and from top to bottom, from 0 to 0.9 s.

4.5 Simulation of correlated within-event residuals

The fitted covariance model provides the basis for two complementary simulation modes: (i) unconditional simulation, used to generate spatially correlated residual fields for scenario events, and (ii) conditional simulation, used to generate realizations anchored to observed station residuals for reconstructing historical events. In this section we provide a brief description of both simulation methods, which are detailed in the Supplemental Material.

4.5.1 Unconditional simulation

To generate spatially, inter-period, and inter-component correlated short-period residual fields consistent with the fitted nested LMC, we simulate a multivariate, zero-mean Gaussian random field for the normalized within-event residuals $\boldsymbol{\varepsilon}(\mathbf{s}) \in \mathbb{R}^p$, with spatial covariance represented by Eq. 9. Unconditional realizations are obtained by independently simulating the three Gaussian components of the LMC model and summing them, then scaling back to ln-units using the heteroskedastic within-event standard deviations in Eq. 3

$$\boldsymbol{\delta W_{es}} = \boldsymbol{\varepsilon_u}(\mathbf{s}) \odot \boldsymbol{\phi}(\boldsymbol{M_w}), \quad \mathbf{Y}^{\mathrm{sim}}(\mathbf{s}) = \mathbf{Y}^{\mathrm{ANN}}(\mathbf{s}) + \boldsymbol{\delta W_{es}}, \tag{13}$$

where $\odot$ denotes elementwise multiplication, subindex u refers to unconditional simulation, and $\mathbf{Y}^{\mathrm{ANN}}$ are the ANN predictions in ln-units (see Eq. 1).

For large numbers of sites N, the direct approach (forming the full $N \times N$ correlation matrices and applying Cholesky factors) becomes impractical. We therefore optionally replace the exact correlation operators with scalable approximations: a Vecchia/nearest-neighbour approximation for the short-range component [73,74] and a Nyström low-rank approximation for long-range correlations [75].

4.5.2 Conditional simulation

To generate fields conditioned on recorded ground motions at a subset of sites, we implement the "unconditional draw + deterministic conditioning correction" approach described in Hoffman [76]. Given an unconditional realization $\boldsymbol{\varepsilon_u}(\mathbf{s})$ obtained as described in Appendix A, the conditioned field of normalized residuals is obtained as

$$\boldsymbol{\varepsilon_c}(\mathcal{U}) = \boldsymbol{\varepsilon_u}(\mathcal{U}) + \mathbf{C}_{\mathcal{U}\mathcal{O}}\, \mathbf{C}_{\mathcal{O}\mathcal{O}}^{-1}\big(\boldsymbol{\varepsilon_{obs}}(\mathcal{O}) - \boldsymbol{\varepsilon_u}(\mathcal{O})\big), \tag{14}$$

where $\mathcal{O}$ and $\mathcal{U}$ are observed and unobserved sites, respectively. This ensures that $\boldsymbol{\varepsilon_c}(\mathcal{U})$ are consistent with the observed data, while preserving the spatial correlation structure of the unconditional random field. The simulated field $\mathbf{Y}^{\mathrm{sim}}(\mathbf{s})$ is obtained from Eq. 13 using $\boldsymbol{\varepsilon_c}(\mathbf{s})$.

5 Simulation of broadband time histories

Ground motions from PBS are valid only up to a certain frequency f_{max}, dependent on the resolution of the numerical model, however, BB time histories are needed for engineering applications. BB ground motions can be generated as follows

(1) simulation of BB cross-correlated response spectra as described in the previous section;

(2) simulation of a non-stationary stochastic (STO) accelerogram per monitor and per component. We follow an approach similar to Sabetta et al. [37], and including coherency between horizontal components defined from the model of Hong and Liu [77]. The parameters of the stochastic time envelope are computed from each PBS low-frequency signal, consequently, the onset and duration of the stochastic signals is similar to that of the PBS signals;

(3) BB signals are created by merging STO signals with the PBS signals in the frequency domain using complementary low-pass/high-pass filters, with a transition band centred at a frequency near but below f_{max};

(4) Spectral matching with a PGA correction similar to the method of Liu et al. [78] is then applied to match the target SA from step (1);

(5) since spectral matching can add some displacement drift, the adjusted BB signals are re-merged with the PBS signals to preserve the LF content and any permanent displacement captured by the PBS; and

(6) steps 4 and 5 are repeated until the mismatch between target and BB SA falls below a prescribed threshold.

6 Application case study: South Iceland

In this section we present the results from the application of the proposed broadband generation procedure for two PBS of earthquakes of M_w 6.5 and 6.4 carried out by Hernández-Aguirre et al.[36]. This represents a demanding test case, given the limited frequency content of the physics-based simulations and the sparse strong-motion dataset available for regional calibration. The results presented are not limited to median trends, but we analyze also directionality, inter-period and spatial correlation, which are relevant for seismic hazard and risk applications.

6.1 Physics-based simulations for South Iceland

We use results of regional three-dimensional PBS of seismic wave propagation for the M_w 6.5 and M_w 6.4 June 2000 South Iceland earthquakes generated by [36]. Their numerical model of South Iceland (138 × 90 × 25 km^3) was developed with a spatial resolution sufficient to propagate frequencies up to ~f_{max}=1.9 Hz. The seismic rupture process was modelled using a kinematic rupture procedure that incorporates heterogeneous slip, rupture velocity, and peak slip rate as correlated stochastic spatial fields. Results from these simulations are available at 2000 ground surface virtual monitors distributed over the whole domain. For more information about the simulations, we refer the reader to [36], that also discusses the performance of the LF PBS, in comparison with available records, while here we focus on the BB results.

6.2 BB time histories

Times series from the simulations were low-pass filtered at 1.9 Hz, in agreement with the maximum resolvable frequency f_{max}. The filtered PBS signals were subsequently processed using the procedure described in the previous section to generate BB ground motions, using conditional simulation of within-event residuals, anchored on recorded values. The complementary merging filters provide a smooth frequency-domain transition between 1.1 and 1.8 Hz. We emphasize that the transition period of the ANN to be used to estimate short period SA should be higher than $1/f_{max}$, since SA($1/f_{max}$) is still affected by frequencies larger than f_{max}, which are not present in the PBS signals due to the low-pass filtering. Accordingly, we used T*=1 s, but values slightly lower or higher gave similar results. If PBS reach higher frequencies, a lower T* could be used.

Figure 11 and Figure S14 compare recorded and simulated BB accelerograms, SA, and Fourier amplitude spectra (FAS) at selected stations for the 17 June 2000 earthquake. This comparison should be interpreted as a conditional reconstruction test rather than as an independent prediction test. The close agreement in SA(T<T*) at recording sites is expected due to the conditional simulation used. The results nevertheless provide a useful check that the broadband reconstruction is compatible with the recorded spectral amplitudes and does not introduce obvious discontinuities around T*. The simulated and recorded motions also show comparable behaviour in the time and frequency domains, including similar significant durations D5-75.

To illustrate the difference between conditional reconstruction and predictive simulation, Figure S15 shows the same stations using an unconditioned residual field. In this case, larger differences are observed in the short-period spectral ordinates because the recorded short-period residuals are not imposed. However, the overall amplitude level, frequency content, and time evolution of the broadband accelerograms remain broadly consistent with the observations. Exact waveform reproduction is not expected in either case because the high-frequency component is stochastic and the PBS are affected by epistemic uncertainty in the source and path models.

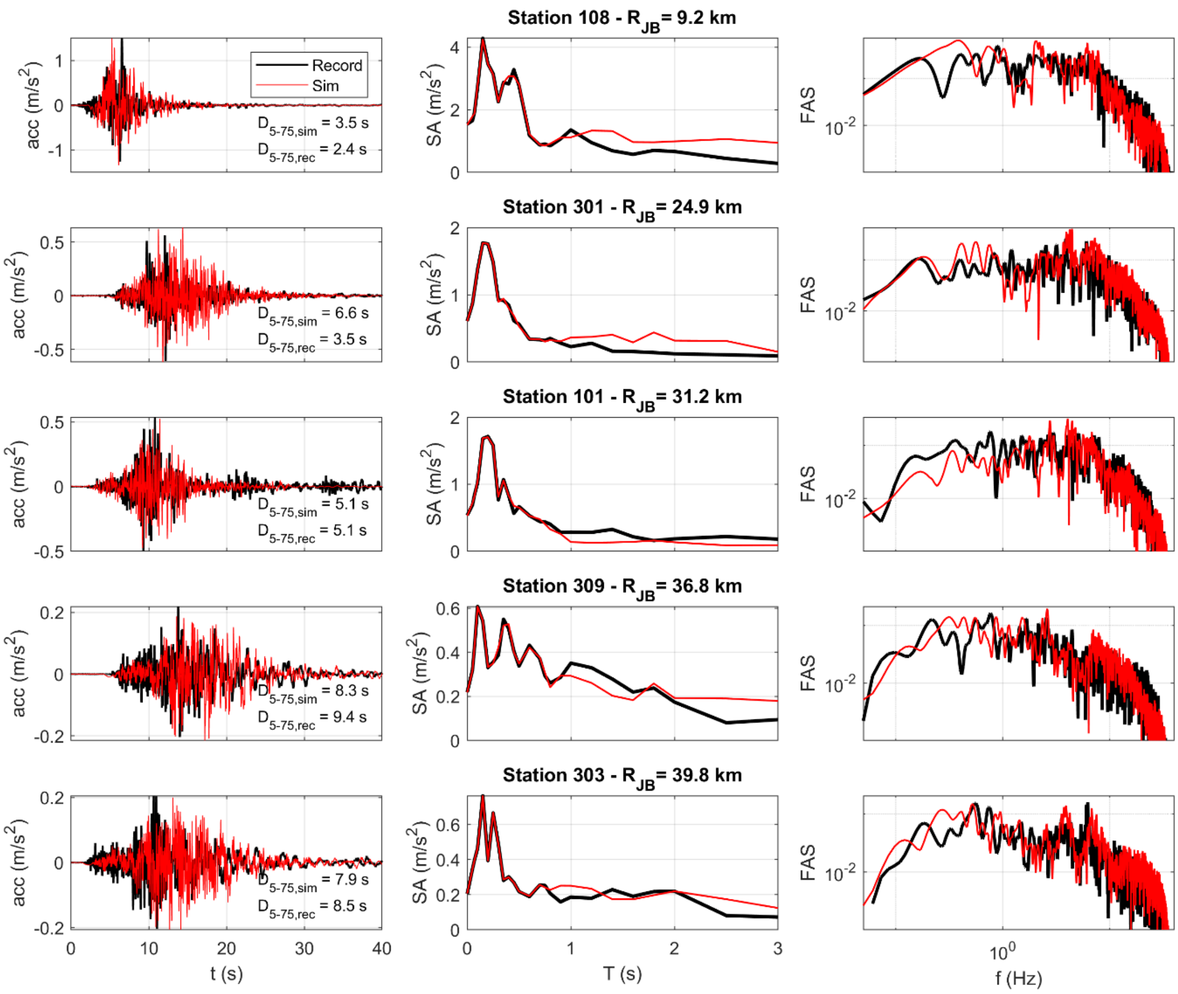

Figure 11. Comparison of recorded and conditionally simulated BB accelerograms, SA, and Fourier amplitude spectra (FAS) at selected stations for the 17 June 2000 earthquake.

6.3 Short period attenuation

Figure 12 shows horizontal RotD50 and vertical SA for different short periods as a function of R_{JB}, from recordings (crosses) and simulations (circles). For the horizontal component we also show the estimates of the GMM by Akkar & Bommer (AB10) [79] (yellow lines), and from the local GMM 'F' by Kowsari et al. (KS20) [80] (red lines). SA from KS20 corresponds to a rotational invariant measure, similar to RotD50 [72]. There is currently no ground motion model for vertical SA in Iceland, so we do not show any GMM for that component. The following observations can be made from these comparisons:

- In general, there is a good agreement between records and simulations in terms of attenuation trends with distance across all examined periods;
- The simulated SAs show the expected near-fault saturation in agreement with GMMs;
- Since the GMM KS20 was calibrated using the IceSMN dataset, of which almost half of the records are from the June 2000 South Iceland earthquakes, this model fits very well the recordings and our simulations;
- The GMM by AB10 underestimates SA at short distances and overestimates it further away from the source, which is usually observed from GMMs calibrated from data outside Iceland [62]. This highlights the usefulness of TL, which allows an ANN to be fine-tuned regional data; and
- Vertical SAs have a scatter and attenuation trend very similar to that shown by records.

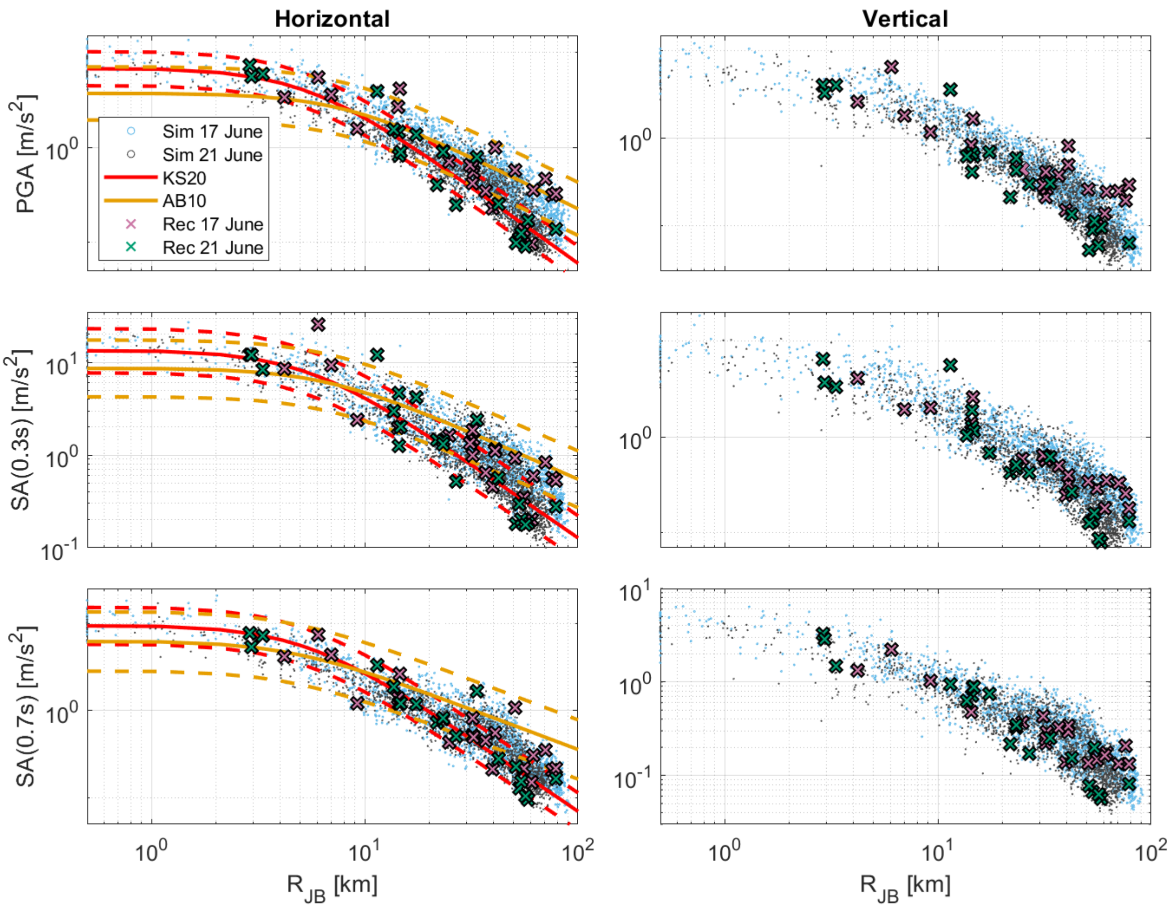

Figure 12. Attenuation of horizontal RotD50 (left) and vertical SA (right) at selected short periods (PGA, 0.3 s and 0.7 s) from recordings (crosses), simulations (circles), and from the GMMs by Akkar & Bommer (AB10) [79] (yellow lines) and Kowsari et al. (KS20) [80] (red lines). Median predictions of the GMMs are shown with solid lines, while median ± one standard deviation are shown with dashed lines.

6.4 Polarization and directionality

Earthquake ground motions display distinctive near-source characteristics [81], such as long-period ground-motion polarization due to rupture directivity and source radiation effects, but such polarization tends to diminish at higher frequencies. Moreover, short-period vertical amplitudes can substantially exceed the horizontal components [82]. By including simultaneously the three components of SA in the ANN, the aim was to preserve physically plausible horizontal polarization and vertical-to-horizontal (V/H) ratios at short periods. In this section we analyse these aspects.

Figure 13 compares maps of fault-normal (FN) to fault-parallel (FP) PGA ratio, for the 21 June 2000 South Iceland earthquake. For the proposed three-component model, the mean FN/FP ratios for short period SAs are close to one at all distances, as expected for short-period motion [81]. In the directivity regions, i.e., towards the north and south along the strike direction, FN/FP tends to be larger, whereas in the perpendicular direction it is the lowest (Figure 13a). This spatial pattern is consistent with expectations from rupture directivity and S-wave radiation effects, indicating that the short-period motions retain physically meaningful directional characteristics inherited from the long-period physics-based simulations, while remaining within realistic amplitude ranges.

For comparison, Figure 13b shows the corresponding result obtained with a GMH-based ANN baseline. In this baseline, a model trained on the geometric mean of the horizontal components is applied separately to each horizontal component, without explicitly modelling cross-component dependence. This produces substantially stronger short-period polarization, with FN/FP PGA ratios reaching values of about five in the directivity regions. The comparison suggests that treating the horizontal components independently can transfer excessive long-period polarization into the short-period range, whereas the proposed joint three-component model better constrains the horizontal component ratios. The median SARotD100 to SARotD50 ratios at various periods from recordings and simulations are compared to the empirical model of Boore and Kishida (BK2017) [80] in Figure 14a. The recordings show ratios slightly larger than the empirical model at all periods, with a trend against period similar to the model. At short periods, the ratio from simulations is similar to the ratio from records, whereas in the physics-based dominated part, above 1 s, it is considerably larger than the empirical model, however, it is close to what observed from records of both earthquakes.

In contrast, the GMH-based ANN baseline produces SARotD100 to SARotD50 ratios at short periods that are substantially larger than those observed in the recordings and predicted by BK2017. This supports the map-based observation that applying a GMH-trained model independently to the two horizontal components can lead to excessive short-period polarization. The joint three-component formulation therefore provides a more physically consistent treatment of horizontal component dependence.

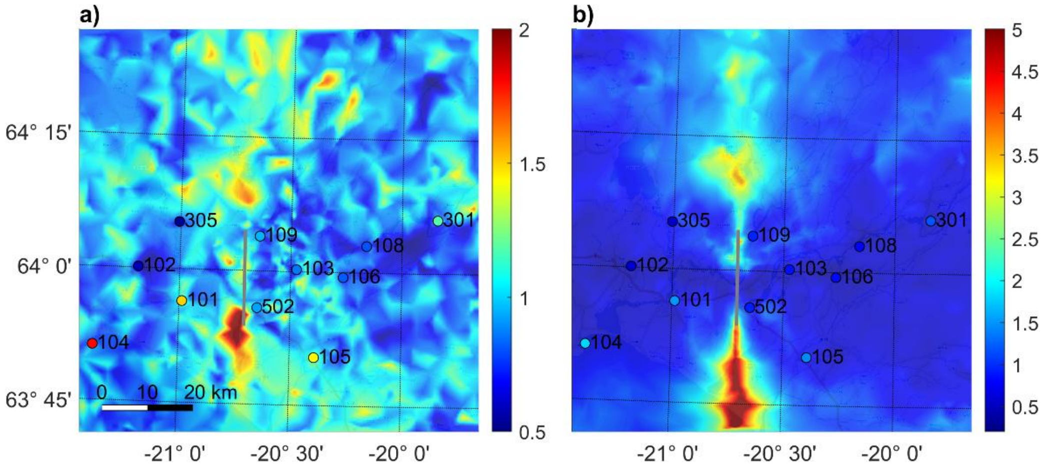

Figure 13. Maps of fault-normal (FN) / fault-parallel (FP) PGA for the 21 June 2000 South Iceland earthquake, from (a) the proposed three-component ANN, and (b) the GMH-based ANN baseline applied independently to the two horizontal components. Circles show recorded values using the same colour scale. The GMH-based baseline produces substantially larger FN/FP ratios in the directivity regions, indicating excessive short-period polarization when horizontal components are treated independently.

Panels b and c of Figure 14 present V/H spectral ratios at two short periods. The horizontal SA are RotD50. Vertical bars denote the mean V/H ratio within discrete distance bins, together with ±1 standard deviation. For comparison, we also plot estimates from the V/H model of Gülerce and Abrahamson (GA2011) [79] for Vs_{30}=760 m/s and a strike-slip event of M_w=6.5. Overall, the simulations are consistent with the empirical model: across all bins, the simulated mean remains within the empirical model median ± one within-event standard deviation. Notably, some locations exhibit V/H ratios exceeding unity, occasionally approaching values close to two. These elevated ratios predominantly occur at locations approximately 45° from the nodal planes of the faulting mechanism, where the S-wave radiation is minimized while the P-wave (producing mostly vertical motion) radiation is maximized, explaining the observed spatial pattern (not shown for brevity).

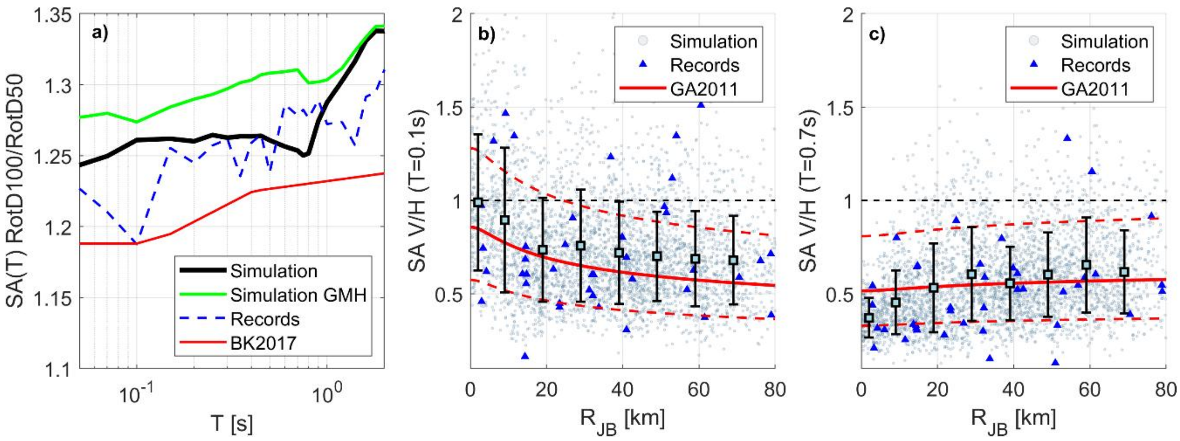

Figure 14. (a) Ratio of SARotD100 to SARotD50 from empirical model of Boore and Kishida (BK2017) [83] and the median ratio from recordings and simulations of the 2000 South Iceland earthquakes. Ratios of vertical to horizontal SA at 0.1 s (b) and 0.7 s (c), from simulations, records, and the model of Gülerce and Abrahamson (GA2011) [79]. The vertical bars represent the mean ± one standard deviation from simulations at various distance bins.

6.5 Inter-period and spatial correlation

Figure 15 shows the correlation coefficients (ρ) between periods T_1 and T_2 of the within-event residuals ε for the two South Iceland earthquakes. Residuals were computed with respect to the local GMM KS20. In general, both simulations follow a trend similar to the empirical model of Baker & Jayaram [21]. The correlation of ε has a smooth transition between the stochastic and physics-based part, indicating that inter-period correlation is preserved across the stochastic–physics-based transition, in contrast to the degradation observed in some earlier hybrid simulation methods [31].

Finally, we computed empirical semivariograms γ(h) from normalized within-event residuals at various periods of the RotD50 SA. Residuals were computed with respect to a simple model fitted to the simulated intensity measures [30]. Then we fitted an exponential model to the semivariograms using the least squares method. The exponential model is defined as $g(h) = a[1 - \exp(-3h/b)]$, where a is the sill, or the population variance of the random field [84], and b is the range, defined as the inter-site distance at which γ(h) reaches 95% of the sill, beyond which spatial correlation can be considered negligible [15]. Figure 16 shows semivariograms for T=0.1 s and T=0.3 s together with the fitted exponential models. It should be noted that $\gamma(0) \neq 0$, as the LMC model includes a nugget term represented by $\mathbf{P}^3$. This term accounts for spatially uncorrelated variability at infinitesimal separation distances, such as site-specific effects, and results in a non-zero semivariance even at zero lag. Then in panel c we show the estimated ranges at various periods, which are similar to those from various empirical models [15,17,85]. Interestingly, the range attains relatively large values around 1 s, which is dominated by the PBS part, potentially reflecting source effects that generate strongly coherent ground motion at those frequencies; however, confirming the physical origin of this behaviour requires further study.

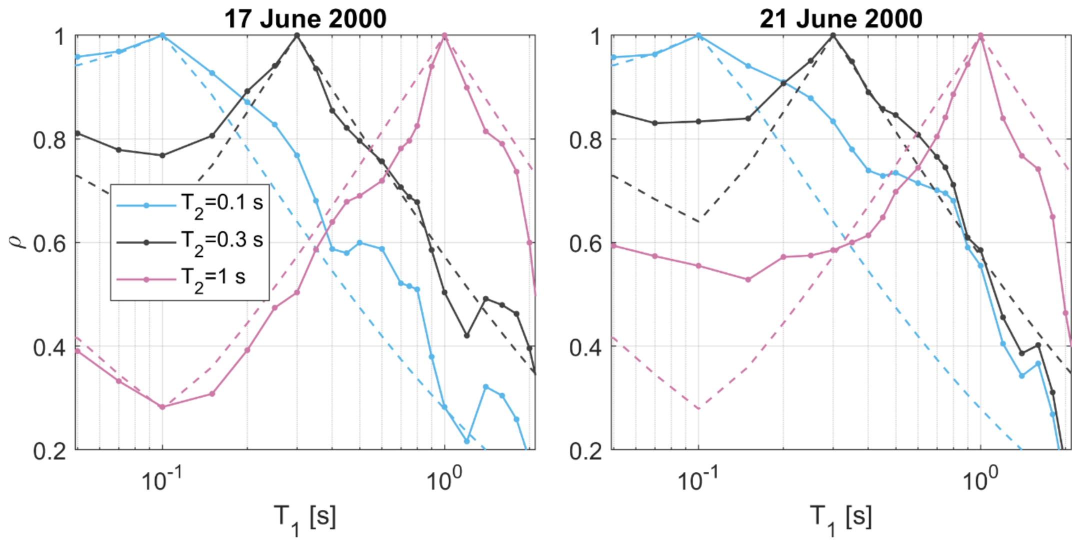

Figure 15. Correlation of ε from simulations of the 2000 South Iceland earthquakes (solid lines), compared with an empirical model (dashed lines) for shallow crustal earthquakes [21], at T_2 =0.1 s, 0.3 s, and 1 s.

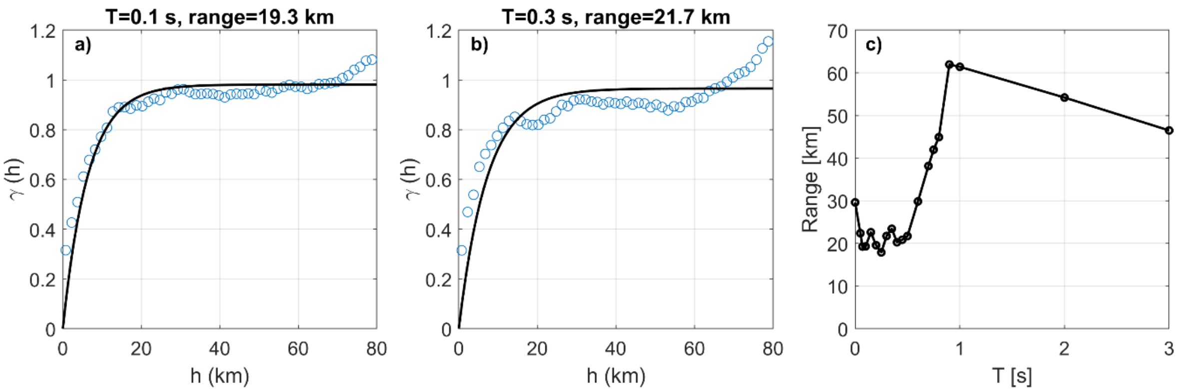

Figure 16. Example empirical semivariograms and fitted exponential models for T=0.1 s (a) and T=0.3 s (b). Spatial correlation ranges estimated for the 21 June 2000 South Iceland simulation (c).

7 Discussion of results

This study presented and validated an enhanced broadband ground-motion generation framework that combines low-frequency PBS, machine-learning predictions of short-period spectral accelerations, and empirically constrained residual correlation modelling. The methodology was applied to two different earthquakes in South Iceland, with M_w 6.5 and 6.4, providing a demanding demonstration case given the limited frequency content of the PBS and the limited ground-motion dataset available for regional calibration. The results should therefore be interpreted as a methodological evaluation for this specific regional application, rather than as a comprehensive validation of the framework.

Overall, the proposed workflow yields broadband ground motions that are consistent with observations across several intensity-measure-based diagnostics, including amplitude scaling, directionality, component ratios, and spatial/inter-period dependence. For the South Iceland case-study, the attenuation of short-period horizontal and vertical SAs with distance is reproduced realistically, including near-fault saturation effects and realistic scatter. The agreement with the local GMM KS20 is useful as a regional consistency check, but it should not be interpreted as independent validation because KS20 was calibrated using the IceSMN dataset, including many records from the June 2000 South Iceland sequence. In this context, KS20 is used as a locally calibrated reference trend against which the regional behaviour of the simulations can be compared.

7.1 Transfer learning

The results indicate that TL enables the ANN to better represent Icelandic attenuation characteristics than the same model trained only with the global dataset, supporting the use of regional fine-tuning in data-limited environments. At magnitudes that are poorly represented in the local Icelandic dataset, the fine-tuned model relies primarily on the magnitude-scaling trends learned from the larger global dataset, while the Icelandic records provide a regional adjustment to attenuation and site effects. Such applications should therefore be interpreted cautiously, but they are not extrapolations from the limited Icelandic dataset alone.

For applications to other regions, an important practical question is how much target-region data is needed for stable transfer learning. To address this issue, we performed a TL data-size sensitivity analysis. The pretrained global ANNs were fine-tuned using increasing fractions of the local Icelandic dataset, from 50% to 100% of the available records. For each fraction, five independently trained networks were evaluated, and the mean validation and test RMSE and bias were computed.

The results in Figure S16 show that using larger fractions of the local dataset generally reduces both RMSE and absolute bias consistently for the two subsets, indicating a more stable regional calibration. The trend is not strictly monotonic, which is expected given the limited size of the local dataset and the sensitivity of the validation/test subsets to the specific records included in each split. Nevertheless, the full-data case provides the most consistent overall performance, with both lower RMSE and bias close to zero. These results suggest that, for the present application, using substantially fewer local records than available would not be advisable. However, this should not be interpreted as a universal threshold, because the required amount of target-region data depends on the coverage of magnitude, distance, site conditions, and long-period spectral amplitudes. For applications with fewer records, a more restrictive fine-tuning strategy, such as updating only the output layers, should be preferred to reduce the risk of overfitting.

7.2 Directionality and Component Consistency

Beyond median attenuation trends, the framework preserves physically meaningful directionality and polarization characteristics in the South Iceland case study. These diagnostics are relevant for near-fault engineering applications. The spatial pattern of FN over FP PGA is consistent with expectations from rupture directivity and radiation effects. While average FN/FP ratios at short periods remain close to unity, the simulations capture spatial variability, including larger ratios in directivity regions.

The RotD100/RotD50 ratios exhibit a coherent transition from stochastic-dominated to physics-dominated regimes. At short periods, simulated ratios track the empirical model of Boore and Kishida [83]; within the transition band they increase toward the levels observed in the recordings; and at longer periods they reflect stronger polarization driven by the PBS, consistent with the data for both earthquakes. Similarly, the vertical-to-horizontal (V/H) ratios align well with the model of Gülerce and Abrahamson [82], including localized exceedances of unity associated with radiation-pattern effects.

These results indicate that jointly training the ANN on three components helps preserve realistic component-to-component relationships. The comparison with the GMH-based baseline further supports this interpretation: when the horizontal components are predicted independently, short-period polarization is overestimated, whereas the joint three-component ANN keeps FN/FP and RotD100/RotD50 ratios closer to observed and empirical ranges.

7.3 Inter-Period and Spatial Correlation

A key contribution of this work is the explicit and unified treatment of inter-period, spatial and cross-component correlation of within-event residuals. For the two South Iceland simulations considered here, the inter-period correlation structure inferred from the simulated motions closely follows the empirical model of Baker and Jayaram [21], with a smooth transition across the stochastic–physics-based boundary. This behaviour contrasts with earlier hybrid broadband procedures where correlations may degrade near the transition frequency, and suggests that the combined ANN + correlated-residual approach can provide a consistent statistical bridge across frequency regimes.

Spatial correlation analysis yields correlation ranges broadly consistent with published empirical models. The presence of a nugget effect is physically plausible and reflects spatially uncorrelated variability (e.g., unresolved site-specific effects and modelling uncertainty), leading to a non-zero semivariance at zero separation. The observation of relatively large correlation ranges around ~1 s is particularly noteworthy and may reflect enhanced source-controlled coherence at intermediate periods for this specific case-study; however, confirming the physical origin of this feature requires additional study.

7.4 Implications for Hazard and Risk Applications

From an engineering perspective, the framework provides a practical way to generate broadband ground-motion fields that are spectrally compatible and statistically consistent across space, periods, and components. These characteristics are relevant for scenario-based hazard and risk analyses, especially for applications involving spatially distributed infrastructure, portfolios, or vector-valued intensity measures. Importantly, the approach is computationally efficient: once the ANN is trained, broadband time histories can be generated rapidly for large scenario sets and dense spatial grids.

However, the present study verifies these properties mainly at the level of intensity measures and their correlation structure. It does not constitute a full engineering validation in terms of nonlinear structural response, portfolio loss, or code-based design quantities. Accordingly, the proposed framework should be viewed as a potential tool for generating input ground-motion fields for scenario-based hazard and risk studies, subject to additional validation for the specific application of interest. In particular, engineering-level validation using single-degree-of-freedom and multi-degree-of-freedom structural response [31,86,87], damage measures, or portfolio loss metrics remains an important step before using the generated motions in design-oriented workflows.

The framework also provides a practical mechanism to represent aleatory variability conditional on the selected PBS input. Aleatory uncertainty can be explored by generating multiple realizations of the correlated within-event residual field, while long-period source and path variability can be sampled through alternative PBS rupture realizations. However, epistemic uncertainty in the PBS model itself, including uncertainty in the 3-D velocity structure, attenuation model, and rupture parametrization, is not removed by the ANN and should be considered separately in project-specific applications.

7.5 Limitations

Despite the encouraging results, several limitations should be acknowledged.

(i) Reliance on empirical data. The methodology is fundamentally data-driven. Both the ANN predictions at short periods and the residual correlation model depend on empirical strong-motion observations. Consequently, performance may degrade when extrapolating to conditions that are weakly represented in the available datasets. The ANN is designed to reproduce statistical trends and variability in intensity measures, rather than to reconstruct a unique physical realization of the short-wavelength field.

(ii) Bounded magnitude and regional validation. The global ANN was trained using crustal earthquake records with magnitudes up to M_w 7.8; therefore, the model should not be used beyond this range without additional validation. The South Iceland application presented here involves two strike-slip earthquakes with M_w 6.4–6.5 in a single region. Thus, although the global training dataset includes larger-magnitude records, the complete broadband workflow has not been independently evaluated here for $M_w > 7$ events or for other tectonic settings. Applications outside the demonstrated magnitude and regional range should therefore be treated as extrapolations unless supported by additional validation. Larger-magnitude applications are being investigated in companion work, but they are outside the validation scope of the present paper.

(iii) Lack of explicit high-frequency wave propagation physics. High-frequency motion is introduced through stochastic/ML-driven components constrained to match observations, but the framework does not explicitly simulate high-frequency wave propagation, including detailed scattering, small-scale 3-D heterogeneity, and fine-scale site effects. In an ideal setting, fully physics-based broadband simulations would directly propagate energy to high frequencies while simultaneously reproducing realistic spatial and cross-period/cross-component correlations. At present, however, regional PBS are computationally constrained in $f_{\max}$, and achieving both very high frequencies and dependence structures consistent with observations remains challenging. The proposed approach should therefore be viewed as a practical compromise: physics-based where feasible at long periods and empirically constrained where necessary at short periods.

(iv) Empirical nature and transferability of the correlation model. For simplicity, the residual correlation model adopted here does not depend explicitly on region, magnitude, or site class. Although this assumption is partly supported by studies reporting weak or inconsistent dependence of spatial and inter-period correlations on these variables, event-to-event and regional variability may still be important. The estimated nugget, sill, and range parameters should therefore be interpreted as average empirical properties of the calibration dataset, and applying the same correlation structure outside this context should be done cautiously and preferably supported by additional validation.

(v) Dependence on the accuracy of the underlying PBS. Since the ANN conditions the short-period response on long-period PBS ordinates, systematic errors in the velocity model, attenuation structure, source characterization, or rupture kinematics are not removed by the network and may be transferred, or in some cases amplified, in the high-frequency predictions. Validation of the PBS against available recordings is therefore a prerequisite for applying the proposed workflow.

8 Conclusions and Outlook

Within the scope of the South Iceland case study, the proposed broadband generation procedure reproduces observed attenuation trends at short periods, preserves physically plausible directionality and component ratios, and yields inter-period and spatial correlation structures that are consistent with empirical models and do not exhibit an artificial loss of correlation at the stochastic–PBS transition. These results support the use of the framework as a methodological basis for generating spatially and spectrally coherent broadband ground-motion fields.

Future work should expand the validation to additional events, regions, and magnitude ranges, including larger-magnitude scenarios, and should explore sensitivity to PBS configuration, rupture modelling choices, and epistemic uncertainty in the 3D velocity model. Further work should also investigate the physical mechanisms controlling period-dependent spatial correlation. Finally, engineering-level validation should be performed using engineering demand parameters, as well as quantitative seismic damage or loss evaluations on building portfolios.

Overall, the results indicate that combining physics-based simulations, transfer learning, and empirically constrained residual correlation modelling provides a promising and computationally efficient pathway for broadband ground-motion simulation. However, the framework should be applied within its demonstrated domain of applicability, and additional validation is required before using it for design-level or regulatory applications.

Acknowledgements

This work was financed by the SERICE project funded by a Grant of Excellence from the Icelandic Centre for Research (RANNIS), Grant Number: 218149-051. The Authors from Politecnico di Milano acknowledge funding from ReLUIS (Rete dei Laboratori Universitari di Ingegneria Sismica), in the framework of the WP18 work package “Input sismico, normativa e microzonazione”, within the DPC (Dipartimento della Protezione Civile)-ReLUIS Agreement 2024–2026. The constructive comments of two anonymous reviewers have significantly contributed to the paper improvement.

Data Availability Statement The trained ANN models, train/validation/test data, and code required to train new models are archived on Zenodo under DOI: 10.5281/zenodo.20668084. The ground motion records used for training the ANN model were obtained the following databases: Engineering Strong-Motion (ESM, https://esm-db.eu/, last accessed November 2025), Pacific Earthquake Engineering Research Center (PEER) NGA-West2 (https://ngawest2.berkeley.edu/, last accessed December 2020).

References

1. McCallen D, Pitarka A, Tang H, et al. Regional-Scale Fault-to-Structure Earthquake Simulations with the EQSIM Framework: Workflow Maturation and Computational Performance on GPU-accelerated Exascale Platforms. *Earthquake Spectra*. 2024;40(3):1615-1652. doi:10.1177/87552930241246235
2. Paolucci R, Mazzieri I, Piunno G, Smerzini C, Vanini M, Özcebe AG. Earthquake Ground Motion Modeling of Induced Seismicity in the Groningen Gas Field. *Earthquake Engineering and Structural Dynamics*. 2021;50(1):135-154. doi:10.1002/eqe.3367
3. Smerzini C, Vanini M, Paolucci R, Renault P, Traversa P. Regional Physics-Based Simulation of Ground Motion within the Rhone Valley, France, during the Mw 4.9 2019 Le Teil Earthquake. *Bulletin of Earthquake Engineering*. 2023;21(4):1747-1774. doi:10.1007/s10518-022-01591-w
4. Hanks TC, McGuire RK. The Character of High-Frequency Strong Ground Motion. *Bulletin of the Seismological Society of America*. 1981;71(6):2071-2095.
5. Motazedian D, Atkinson GM. Stochastic Finite-Fault Modeling Based on a Dynamic Corner Frequency. *Bulletin of the Seismological Society of America*. 2005;95(3):995-1010. doi:10.1785/0120030207
6. Boore DM. Simulation of Ground Motion Using the Stochastic Method. *Pure and Applied Geophysics*. 2003;160(3):635-676. doi:10.1007/PL00012553
7. Douglas J, Aochi H. A Survey of Techniques for Predicting Earthquake Ground Motions for Engineering Purposes. *Surveys in Geophysics*. 2008;29(3):187-220. doi:10.1007/s10712-008-9046-y
8. Graves R, Pitarka A. Broadband ground-motion simulation using a hybrid approach. *Bulletin of the Seismological Society of America*. 2010;100(5 A):2095-2123. doi:10.1785/0120100057
9. Crempien JGF, Archuleta RJ. UCSB Method for Simulation of Broadband Ground Motion from Kinematic Earthquake Sources. *Seismological Research Letters*. 2015;86(1):61-67. doi:10.1785/0220140103
10. Wu M, Ba Z, Liang J. A procedure for 3D simulation of seismic wave propagation considering source-path-site effects: Theory, verification and application. *Earthquake Engineering & Structural Dynamics*. 2022;51:2925-2955. doi:10.1002/eqe.3708
11. Aquib TA, Mai PM. Broadband Ground-Motion Simulations with Machine-Learning-Based High-Frequency Waves from Fourier Neural Operators. *Bulletin of the Seismological Society of America*. 2024;114(6):2846-2868. doi:10.1785/0120240027
12. Gatti F, Clouteau D. Towards Blending Physics-Based Numerical Simulations and Seismic Databases Using Generative Adversarial Network. *Computer Methods in Applied Mechanics and Engineering*. 2020;372. doi:10.1016/j.cma.2020.113421
13. Paolucci R, Gatti F, Infantino M, Smerzini C, Özcebe AG, Stupazzini M. Broadband ground motions from 3D physics-based numerical simulations using artificial neural networks. *Bull Seismol Soc Am*. 2018;108(3):1272-1286. doi:10.1785/0120170293
14. Ba Z, Lyu L, Jingxuan Z, Zhang Y, Wang Y. Predicting the seismic ground-motion parameters: 3D physics-based numerical simulations combined with artificial neural networks. *Earthquake Spectra*. 2024;40:2623-2650. doi:10.1177/87552930241255953
15. Esposito S, Iervolino I. Spatial Correlation of Spectral Acceleration in European Data. *Bulletin of the Seismological Society of America*. 2012;102(6):2781-2788. doi:10.1785/0120120068
16. Goda K, Hong HP. Spatial Correlation of Peak Ground Motions and Response Spectra. *Bulletin of the Seismological Society of America*. 2008;98(1):354-365. doi:10.1785/0120070078
17. Jayaram N, Baker JW. Correlation model for spatially distributed ground-motion intensities. *Earthq Engng Struct Dyn*. 2009;38(15):1687-1708. doi:10.1002/eqe.922
18. Loth C, Baker JW. A spatial cross-correlation model of spectral accelerations at multiple periods. *Earthq Engng Struct Dyn*. 2013;42(3):397-417. doi:10.1002/eqe.2212
19. Abrahamson NA, Silva WJ, Kamai R. Summary of the ASK14 Ground Motion Relation for Active Crustal Regions. *Earthquake Spectra*. 2014;30(3):1025-1055. doi:10.1193/070913EQS198M
20. Baker JW, Bradley BA. Intensity Measure Correlations Observed in the NGA-West2 Database, and Dependence of Correlations on Rupture and Site Parameters. *Earthquake Spectra*. 2017;33(1):145-156. doi:10.1193/060716eqs095m
21. Baker JW, Jayaram N. Correlation of Spectral Acceleration Values from NGA Ground Motion Models. *Earthquake Spectra*. 2008;24(1):299-317. doi:10.1193/1.2857544
22. Bayless J, Abrahamson NA. Evaluation of the Interperiod Correlation of Ground-Motion Simulations. *Bulletin of the Seismological Society of America*. 2018;108(6):3413-3430. doi:10.1785/0120180095
23. Stafford PJ. Interfrequency Correlations among Fourier Spectral Ordinates and Implications for Stochastic Ground-Motion Simulation. *Bulletin of the Seismological Society of America*. 2017;107(6):2774-2791. doi:10.1785/0120170081

24. Wang N, Olsen KB, Day SM. A Frequency-Dependent Ground-Motion Spatial Correlation Model of within-Event Residuals for Fourier Amplitude Spectra. *Earthquake Spectra*. 2021;37(3):2041-2065. doi:10.1177/8755293020981995
25. Bora SS. Cross-Correlations Between Fourier Spectral Ordinates and Ground-Motion Intensity Measures: An Empirical Study Using the NGA-West2 Database. *Earthquake Spectra*. 2026;42(1):e70033. doi:10.1002/esp4.70033
26. Goda K, Atkinson GM. Probabilistic Characterization of Spatially Correlated Response Spectra for Earthquakes in Japan. *Bulletin of the Seismological Society of America*. 2009;99(5):3003-3020. doi:10.1785/0120090007
27. Park J, Bazzurro P, Baker JW. Modeling spatial correlation of ground motion Intensity Measures for regional seismic hazard and portfolio loss estimation. In: *Applications of Statistics and Probability in Civil Engineering*. Taylor & Francis Group, London; 2007.
28. Weatherill GA, Silva V, Crowley H, Bazzurro P. Exploring the impact of spatial correlations and uncertainties for portfolio analysis in probabilistic seismic loss estimation. *Bull Earthquake Eng*. 2015;13(4):957-981. doi:10.1007/s10518-015-9730-5
29. Chen Y, Baker JW. Spatial Correlations in Cybershake Physics-Based Ground-Motion Simulations. *Bulletin of the Seismological Society of America*. 2019;109(6):2447-2458. doi:10.1785/0120190065
30. Infantino M, Smerzini C, Lin J. Spatial Correlation of Broadband Ground Motions from Physics-Based Numerical Simulations. *Earthquake Engineering and Structural Dynamics*. 2021;50(10):2575-2594. doi:10.1002/eqe.3461
31. Burks LS, Baker JW. Validation of Ground-Motion Simulations through Simple Proxies for the Response of Engineered Systems. *Bulletin of the Seismological Society of America*. 2014;104(4):1930-1946. doi:10.1785/0120130276
32. Kubo H, Naoi M, Kano M. Recent advances in earthquake seismology using machine learning. *Earth Planets Space*. 2024;76(1):36. doi:10.1186/s40623-024-01982-0
33. Pan SJ, Yang Q. A Survey on Transfer Learning. *IEEE Transactions on Knowledge and Data Engineering*. 2010;22(10):1345-1359. doi:10.1109/TKDE.2009.191
34. Jozinović D, Lomax A, Štajduhar I, Michelini A. Transfer Learning: Improving Neural Network Based Prediction of Earthquake Ground Shaking for an Area with Insufficient Training Data. *Geophysical Journal International*. 2022;229(1):704-718. doi:10.1093/gji/ggab488
35. Sreenath V, Basu J, Raghukanth STG. Ground Motion Models for Regions with Limited Data: Data-driven Approach. *Earthquake Engineering & Structural Dynamics*. 2024;53(3):1363-1375. doi:10.1002/eqe.4075
36. Hernández-Aguirre VM, Rupakhety R, Paolucci R, et al. A kinematic rupture generator for ground-motion simulations: Validation and scenarios in South Iceland. *EarthArXiv*. Published online 2026. doi:10.31223/X5D776
37. Sabetta F, Pugliese A, Fiorentino G, Lanzano G, Luzi L. Simulation of Non-Stationary Stochastic Ground Motions Based on Recent Italian Earthquakes. *Bulletin of Earthquake Engineering*. 2021;19(9):3287-3315. doi:10.1007/s10518-021-01077-1
38. Paolucci R, Smerzini C, Vanini M. BB-speedset: A validated dataset of broadband near-source earthquake ground motions from 3d physics-based numerical simulations. *Bulletin of the Seismological Society of America*. 2021;111(5):2527-2545. doi:10.1785/0120210089
39. Sgobba S, Felicetta C, Lanzano G, Ramadan F, D'Amico M, Pacor F. NESS2.0: An Updated Version of the Worldwide Dataset for Calibrating and Adjusting Ground-Motion Models in Near Source. *Bulletin of the Seismological Society of America*. 2021;111(5):2358-2378. doi:10.1785/0120210080
40. Graves R, Pitarka A. Kinematic Ground-Motion Simulations on Rough Faults Including Effects of 3D Stochastic Velocity Perturbations. *Bulletin of the Seismological Society of America*. 2016;106(5):2136-2153. doi:10.1785/0120160088
41. Imperatori W, Mai PM. Broad-band near-field ground motion simulations in 3-dimensional scattering media. *Geophysical Journal International*. 2013;192(2):725-744. doi:10.1093/gji/ggs041
42. Bishop CM. *Neural Networks for Pattern Recognition*. Oxford University Press; 1995. doi:10.1093/oso/9780198538493.001.0001
43. Rumelhart DE, Hinton GE, Williams RJ. Learning representations by back-propagating errors. *Nature*. 1986;323(6088):533-536. doi:10.1038/323533a0
44. Hornik K, Stinchcombe M, White H. Multilayer feedforward networks are universal approximators. *Neural Networks*. 1989;2(5):359-366. doi:10.1016/0893-6080(89)90020-8
45. Prechelt L. Early stopping — but when? In: Montavon G, Orr GB, Müller KR, eds. *Neural Networks: Tricks of the Trade: Second Edition*. Springer Berlin Heidelberg; 2012:53-67. doi:10.1007/978-3-642-35289-8_5

46. Sharma V, Dhanya J, Gade M, Sivasubramonian J. New Generalized ANN-based Hybrid Broadband Response Spectra Generator Using Physics-based Simulations. *Natural Hazards*. 2023;116(2):1879-1901. doi:10.1007/s11069-022-05746-5
47. Choudhary R, Sharma V, Dhanya J. Hybrid broadband ground motion generator for data-sparse regions. *Georisk: Assessment and Management of Risk for Engineered Systems and Geohazards*. Published online October 9, 2025:1-24. doi:10.1080/17499518.2025.2569548
48. Fayaz J, Xiang Y, Zareian F. Generalized ground motion prediction model using hybrid recurrent neural network. *Earthq Engng Struct Dyn*. 2021;50(6):1539-1561. doi:10.1002/eqe.3410
49. Luzi L, Puglia R, Russo E, et al. The Engineering Strong-Motion Database: A Platform to Access Pan-European Accelerometric Data. *Seismological Research Letters*. 2016;87(4):987-997. doi:10.1785/0220150278
50. Ancheta TD, Darragh RB, Stewart JP, et al. NGA-West2 Database. *Earthquake Spectra*. 2014;30(3):989-1005. doi:10.1193/070913EQS197M
51. The MathWorks Inc. MATLAB version: 24.2 (R2024b). Published online 2024. https://www.mathworks.com
52. Kingma DP, Ba J. Adam: a method for stochastic optimization. In: 2015. doi:https://doi.org/10.48550/arXiv.1412.6980
53. Huber PJ. Robust estimation of a location parameter. In: Kotz S, Johnson NL, eds. *Breakthroughs in Statistics: Methodology and Distribution*. Springer New York; 1992:492-518. doi:10.1007/978-1-4612-4380-9_35
54. Sreenath V, Gatti F, Jehel P. Breaking the Black Box: Inherently Interpretable Physics-Constrained Machine Learning With Weighted Mixed-Effects for Imbalanced Seismic Data. *Journal of Geophysical Research: Machine Learning and Computation*. 2025;2(4):e2025JH000974. doi:10.1029/2025JH000974
55. Lanzano G, Luzi L, Pacor F, et al. A Revised Ground-Motion Prediction Model for Shallow Crustal Earthquakes in Italy. *Bulletin of the Seismological Society of America*. 2019;109(2):525-540. doi:10.1785/0120180210
56. Au Q, Herbinger J, Stachl C, Bischl B, Casalicchio G. Grouped feature importance and combined features effect plot. *Data Min Knowl Disc*. 2022;36(4):1401-1450. doi:10.1007/s10618-022-00840-5
57. Ramadan F, Smerzini C, Lanzano G, Pacor F. An Empirical Model for the Vertical-to-Horizontal Spectral Ratios for Italy. *Earthquake Engineering and Structural Dynamics*. 2021;50(15):4121-4141. doi:10.1002/eqe.3548
58. Sedaghati F, Pezeshk S. Machine Learning–Based Ground Motion Models for Shallow Crustal Earthquakes in Active Tectonic Regions. *Earthquake Spectra*. 2023;39(4):2406-2435. doi:10.1177/87552930231191759
59. Lin PS, Lee CT, Cheng CT, Sung CH. Response spectral attenuation relations for shallow crustal earthquakes in Taiwan. *Engineering Geology*. 2011;121(3-4):150-164. doi:10.1016/j.enggeo.2011.04.019
60. Al Atik L, Abrahamson N, Bommer JJ, Scherbaum F, Cotton F, Kuehn NM. The Variability of Ground-Motion Prediction Models and Its Components. *Seismological Research Letters*. 2010;81(5):794-801. doi:10.1785/gssrl.81.5.794
61. Rupakhety R, Ólafsson S. IceSMN Icelandic Strong Motion Network [Data Set]. *International Federation of Digital Seismograph Networks*. Published online 2015. doi:10.7914/YW8C-NY36
62. Ólafsson S, Sigbjörnsson R. Attenuation in Iceland Compared with Other Regions. In: *First European Conference on Earthquake Engineering and Seismology (1ECEES)*. 2006.
63. Hernández-Aguirre VM, Rupakhety R, Ólafsson S, et al. Strong Ground Motion from the Seismic Swarms Preceding the 2021 and 2022 Volcanic Eruptions at Fagradalsfjall, Iceland. *Bulletin of Earthquake Engineering*. 2023;21(10):4707-4730. doi:10.1007/s10518-023-01725-8
64. Bessason B, Kaynia AM. Site amplification in lava rock on soft sediments. *Soil Dynamics and Earthquake Engineering*. 2002;22(7):525-540. doi:10.1016/S0267-7261(02)00035-0
65. Olafsdottir EA, Erlingsson S, Bessason B. Hybrid non-invasive characterization of soil strata at sites with and without embedded lava rock layers in the South Iceland Seismic Zone. *Bulletin of Engineering Geology and the Environment*. 2023;82(4). doi:10.1007/s10064-023-03136-0
66. Darzi A, Halldorsson B, Cotton F, Rahpeyma S. Nationwide Frequency-Dependent Seismic Site Amplification Models for Iceland. *Soil Dynamics and Earthquake Engineering*. 2024;183. doi:10.1016/j.soildyn.2024.108798
67. Li X, Grandvalet Y, Davoine F. A baseline regularization scheme for transfer learning with convolutional neural networks. *Pattern Recognition*. 2020;98:107049. doi:10.1016/j.patcog.2019.107049
68. Markhvida M, Ceferino L, Baker JW. Modeling spatially correlated spectral accelerations at multiple periods using principal component analysis and geostatistics. *Earthq Engng Struct Dyn*. 2018;47(5):1107-1123. doi:10.1002/eqe.3007

69. Goulard M, Voltz M. Linear coregionalization model: Tools for estimation and choice of cross-variogram matrix. *Mathematical Geology*. 1992;24(3):269-286. doi:10.1007/BF00893750
70. Heresi P, Miranda E. Uncertainty in intraevent spatial correlation of elastic pseudo-acceleration spectral ordinates. *Bull Earthquake Eng*. 2019;17(3):1099-1115. doi:10.1007/s10518-018-0506-6
71. Bayless J, Abrahamson NA. An Empirical Model for the Interfrequency Correlation of Epsilon for Fourier Amplitude Spectra. *Bulletin of the Seismological Society of America*. 2019;109(3):1058-1070. doi:10.1785/0120180238
72. Rupakhety R, Sigbjörnsson R. Rotation-Invariant Measures of Earthquake Response Spectra. *Bulletin of Earthquake Engineering*. 2013;11(6):1885-1893. doi:10.1007/s10518-013-9472-1
73. Datta A, Banerjee S, Finley AO, Gelfand AE. On nearest-neighbor Gaussian process models for massive spatial data. *WIREs Computational Stats*. 2016;8(5):162-171. doi:10.1002/wics.1383
74. Vecchia AV. Estimation and Model Identification for Continuous Spatial Processes. *Journal of the Royal Statistical Society Series B (Methodological)*. 1988;50(2):297-312.
75. Williams C, Seeger M. Using the nyström method to speed up kernel machines. In: Leen T, Dietterich T, Tresp V, eds. *Advances in Neural Information Processing Systems*. Vol 13. MIT Press; 2000.
76. Hoffman Y. Gaussian fields and constrained simulations of the large-scale structure. In: Martinez VJ, Saar E, Gonzales EM, Pons-Borderia MJ, eds. *Data Analysis in Cosmology*. Springer Berlin Heidelberg; 2009:565-583. doi:10.1007/978-3-540-44767-2_17
77. Hong HP, Liu TJ. Assessment of Coherency for Bidirectional Horizontal Ground Motions and Its Application for Simulating Records at Multiple Stations. *Bulletin of the Seismological Society of America*. 2014;104(5):2491-2502. doi:10.1785/0120130241
78. Liu P, Jiang X, Li J, Qu H. An improved time-domain spectral matching algorithm for peak adjustment and convergence efficiency optimization. *Soil Dynamics and Earthquake Engineering*. 2025;197:109530. doi:10.1016/j.soildyn.2025.109530
79. Akkar S, Bommer JJ. Empirical equations for the prediction of PGA, PGV, and spectral accelerations in Europe, the mediterranean region, and the Middle East. *Seismological Research Letters*. 2010;81(2):195-206. doi:10.1785/gssrl.81.2.195
80. Kowsari M, Sonnemann T, Halldorsson B, Hrafnkelsson B, Snæbjörnsson J, Jónsson S. Bayesian inference of empirical ground motion models to pseudo-spectral accelerations of south Iceland seismic zone earthquakes based on informative priors. *Soil Dynamics and Earthquake Engineering*. 2020;132. doi:10.1016/j.soildyn.2020.106075
81. Somerville PG, Smith NF, Graves RW, Services WCF, Abrahamson NA. Modification of Empirical Strong Ground Motion Attenuation Relations to Include the Amplitude and Duration Effects of Rupture Directivity. *Seismological Research Letters*. 1997;68(1):199-222.
82. Gülerce Z, Abrahamson NA. Site-Specific Design Spectra for Vertical Ground Motion. *Earthquake Spectra*. 2011;27(4):1023-1047. doi:10.1193/1.3651317
83. Boore DM, Kishida T. Relations between Some Horizontal-Component Ground-Motion Intensity Measures Used in Practice. *Bulletin of the Seismological Society of America*. 2017;107(1):334-343. doi:10.1785/0120160250
84. Barnes RJ. The variogram sill and the sample variance. *Mathematical Geology*. 1991;23(4):673-678. doi:10.1007/BF02065813
85. Huang C, Galasso C. Ground-motion intensity measure correlations observed in Italian strong-motion records. *Earthq Engng Struct Dyn*. 2019;48(15):1634-1660. doi:10.1002/eqe.3216
86. Galasso C, Zhong P, Zareian F, Iervolino I, Graves RW. Validation of ground-motion simulations for historical events using MDoF systems. *Earthq Engng Struct Dyn*. 2013;42(9):1395-1412. doi:10.1002/eqe.2278
87. Smerzini C, Amendola C, Paolucci R, Bazrafshan A. Engineering Validation of BB-SPEEDset, a Data Set of near-Source Physics-Based Simulated Accelerograms. *Earthquake Spectra*. 2024;40(1):420-445. doi:10.1177/87552930231206766

Supplemental Material

Architecture and hyperparameter sensitivity analysis

Candidate models were trained using the same training, validation, and test partitions, and input variables. The tested configurations included a single-branch model, a lower-capacity multi-branch MLP, the reference multi-branch MLP, a higher-capacity multi-branch MLP, a deeper multi-branch MLP with an additional shared hidden layer, and a variant with 1D convolutional layers (CNN). In the 1D-CNN model, the long-period spectral ordinates were treated as ordered period-dependent inputs and processed by one-dimensional convolutional layers along the period axis; the resulting feature maps were then summarized using global average pooling (GAP) before fusion with the rest of the network. This comparison was included to test whether local spectral-shape extraction provides a measurable advantage over fully connected spectral branches for the present response-spectrum mapping task. The models were compared in terms of number of trainable parameters, Root Mean Squared Error RMSE and Mean Absolute Error MAE in natural-log units, coefficient of determination R^2, and mean model bias (Table S1).

The sensitivity analysis shows that increasing model complexity beyond the reference architecture does not provide a robust improvement in validation or test performance. The higher-capacity model and the deeper model produced a reduction in RMSE for the test set of only 1.8% and 1.1%, respectively, while the number of trainable parameters increased significantly. The single-branch model, in which all predictors are concatenated without grouped feature processing, achieved slightly better training performance than the reference model but the test performance improved only marginally. This wider generalization gap suggests that direct concatenation of all predictors increases the ability to fit the training data but does not improve out-of-sample prediction. The lower-capacity and the 1D CNN models had a lower performance than the reference model over all metrics.

Table S 1. Architecture-sensitivity analysis for the ANN model with T*=1 s. Candidate architectures were trained using the same event-wise training/validation/test split, input/output variables, loss function, optimizer, learning-rate schedule, and early stopping criterion. Models are evaluated in terms of number of trainable parameters, RMSE, MAE, R^2, and average bias ratio for one horizontal component (over periods and records). The selected architecture corresponds to model M3, retained in the main analysis.

Model	Description	Number of trainable parameters	RMSE (ln) trn/vld/tst	MAE (ln) trn/vld/tst	R^2 trn/vld/tst	Bias (%) trn/vld/tst
M1	No grouped feature processing: Single-branch MLP, N_1=42, N_2=42	6267	0.541/0.550/0.556	0.412/0.424/0.422	0.911/0.908/0.906	-1.6/2.0/-0.4
M2	Lower capacity: Multi-branch MLP, N_1=6, N_2=26	2827	0.563/0.565/0.571	0.427/0.432/0.431	0.904/0.903/0.902	-1.4/2.2/0.1
M3	Reference model: Multi-branch MLP, N_1=12, N_2=51	6304	0.557/0.562/0.563	0.421/0.430/0.424	0.906/0.904/0.904	-1.4/2.6/-0.2
M4	Higher capacity: Multi-branch MLP, N_1=24, N_2=102	16105	0.550/0.554/0.552	0.415/0.422/0.414	0.908/0.907/0.908	-0.9/2.6/-0.2
M5	Extra shared layer: Deeper multi-branch MLP, N_1=12, N_2=51, N_3=51	8956	0.552/0.555/0.556	0.418/0.424/0.421	0.908/0.907/0.907	-1.7/-2.3/-0.3
M6	Two 1D-CNN with GAP at each spectral branch, N_1=12, N_2=51	7060	0.600/0.603/0.590	0.460/0.467/0.450	0.891/0.890/0.895	-0.4/1.8/1.1
M7	GMH: Multi-branch MLP for geometric mean component, N_1=12, N_2=17	1198	0.288/0.291/0.288	0.401/0.407/0.402	0.911/0.911/0.912	-1.9/0.1/-1.3

Simulation of multivariate LMC residual fields

Random field definition and stacking

Let $\mathbf{s} \in \mathbb{R}^2$denote a site coordinate (e.g., UTM in km). We simulate a multivariate Gaussian random field for the normalized within-event residuals,

$$\boldsymbol{\varepsilon}(\mathbf{s}) = \begin{bmatrix} \boldsymbol{\varepsilon}^{H1}(\mathbf{s}) \\ \boldsymbol{\varepsilon}^{H2}(\mathbf{s}) \\ \boldsymbol{\varepsilon}^{V}(\mathbf{s}) \end{bmatrix} \in \mathbb{R}^p, p = 3n_P, \tag{A1}$$

where each block $\boldsymbol{\varepsilon}^{\boldsymbol{comp}}(\mathbf{s}) \in \mathbb{R}^{n_P}$ corresponds to the set of short-period ordinates (all periods simulated simultaneously). The normalized residuals are defined by period/component-specific heteroscedastic within-event standard deviations $\boldsymbol{\phi}(\boldsymbol{M_w}) \in \mathbb{R}^p$ estimated from mixed-effects residual decomposition. Following the nested LMC structure used in spatial cross-correlation modeling (Loth and Baker 2013) and consistent with the frequency-dependent formulation of Wang et al. (2021), we represent the covariance of $\boldsymbol{\varepsilon}(\mathbf{s})$ as a sum of two spatially correlated components with exponential correlation functions and a nugget component, defined by Eq. 7.

Direct unconditional simulation

For a set of N sites $\{\mathbf{s}_i\}_{i=1}^N$, define the $N \times N$ distance matrix H with entries $H_{ij} = h_{ij} = \| \mathbf{s}_i - \mathbf{s}_j \|$. The two spatial correlation matrices are

$$\mathbf{R}_1 = \left[exp\left(\frac{-3h_{ij}}{R_1}\right)\right]_{i,j=1}^N, \mathbf{R}_2 = \left[exp\left(\frac{-3h_{ij}}{R_2}\right)\right]_{i,j=1}^N. \tag{A2}$$

In the direct implementation, we compute Cholesky factors $\mathbf{L}_\ell \mathbf{L}_\ell^\top \approx \mathbf{R}_\ell$ with a small jitter added to ensure positive definiteness. Likewise, we factor the coregionalization matrices $\mathbf{P}_\ell$ into $\mathbf{B}_\ell \mathbf{B}_\ell^\top$ (using PSD projection if needed). We then simulate three independent Gaussian components using matrix-normal algebra:

$$\boldsymbol{\varepsilon}_1 = (\mathbf{B}_1 \, \mathbf{Z}_1 \, \mathbf{L}_1^\top)^\top, \boldsymbol{\varepsilon}_2 = (\mathbf{B}_2 \, \mathbf{Z}_2 \, \mathbf{L}_2^\top)^\top, \boldsymbol{\varepsilon}_3 = (\mathbf{B}_3 \, \mathbf{Z}_3)^\top, \tag{A3}$$

where $\mathbf{Z}_1, \mathbf{Z}_2, \mathbf{Z}_3 \in \mathbb{R}^{d \times N}$ have i.i.d. standard normal entries. The resulting unconditional normalized field is

$$\boldsymbol{\varepsilon} = \boldsymbol{\varepsilon}_1 + \boldsymbol{\varepsilon}_2 + \boldsymbol{\varepsilon}_3 \in \mathbb{R}^{N \times p}, \tag{A4}$$

with covariance

$$\mathrm{Cov}[\mathrm{vec}(\boldsymbol{\varepsilon})] = \mathbf{P}_1 \otimes \mathbf{R}_1 + \mathbf{P}_2 \otimes \mathbf{R}_2 + \mathbf{P}_3 \otimes \mathbf{I}_N, \tag{A5}$$

where $\otimes$ denotes the Kronecker product and $\mathrm{vec}(\cdot)$ stacks by columns.

Because the subsequent step exponentiates simulated ln-fields back to linear spectral accelerations, extreme Gaussian tails can occasionally yield unrealistically large amplitudes when N is large. As a practical safeguard, we optionally apply a smooth saturation to the normalized field (Winsorization-like):

$$\tilde{\boldsymbol{\varepsilon}} = c \tan \mathrm{h}(\boldsymbol{\varepsilon}/c), \tag{A6}$$

with c set to 2. Finally, the simulated residuals in ln-units are obtained by rescaling with $\boldsymbol{\phi}(\boldsymbol{M_w})$:

$$\boldsymbol{\delta W_{es}} = \tilde{\boldsymbol{\varepsilon}} \odot \boldsymbol{\phi}, \quad \mathbf{Y}^{\mathrm{sim}} = \mathbf{Y}^{\mathrm{ANN}} + \boldsymbol{\delta W_{es}}, \tag{A7}$$

where $\mathbf{Y}^{\mathrm{ANN}} \in \mathbb{R}^{N \times d}$contains the ANN mean predictions ln-units.

Scalable simulation for large N: Vecchia and Nyström approximations

The direct approach requires storing dense $N \times N$ matrices and performing $O(N^3)$ Cholesky factorization, which becomes infeasible for $N \sim 10^4$–10^5. We therefore implement scalable approximations of the correlation operators:

Short-range (Vecchia / nearest-neighbour): For the short-range component $\mathbf{R}_1$, we approximate the joint distribution by a product of low-dimensional conditionals (Vecchia, 1988). In modern form, this yields sparse precision and triangular factors that enable simulation with cost $O(Nm^2)$, where m is the neighbour set size (Datta et al., 2016). This approximation is well suited for rapidly decaying correlations.

Long-range (Nyström low-rank): For long-range correlations $\mathbf{R}_2$, we approximate $\mathbf{R}_2$by a low-rank factorization based on $m \ll N$ landmark points (Williams & Seeger, 2000),

$$\mathbf{R}_2 \approx \mathbf{U}\mathbf{U}^\top, \tag{A8}$$

so that a correlated draw can be generated as $\mathbf{r} \approx \mathbf{U}\mathbf{z}$ with $\mathbf{z} \sim \mathcal{N}(\mathbf{0}, \mathbf{I}_m)$. This reduces memory and computation while preserving the dominant long-range modes. In practice, we combine the short- and long-range approximations in a hybrid manner consistent with the additive LMC decomposition as in Eq. A4.

Conditional simulation by deterministic correction

To condition simulated fields on recorded spectral accelerations, we follow the "unconditional draw + deterministic conditioning correction" method described by Hoffman (2009) for conditional random fields. Let $\mathcal{O}$ be the set of observation indices (size N_o) and $\mathcal{U}$ the set of unobserved sites (size N_u). Given recorded values at $\mathcal{O}$, we compute observed normalized within-event residuals relative to the ANN prediction as

$$\boldsymbol{\varepsilon}_{\text{obs}}(\mathcal{O}) = \left(\mathbf{Y}^{\text{obs}}(\mathcal{O}) - \mathbf{Y}^{\text{ANN}}(\mathcal{O})\right) \oslash \boldsymbol{\phi}(\boldsymbol{M_w}), \tag{A9}$$

where $\oslash$ represents elementwise division. We first generate an unconditional normalized field at all sites $\boldsymbol{\varepsilon}_u(\boldsymbol{s} = \mathcal{O} \cup \mathcal{U})$ as described before. Define the mismatch at observed sites as

$$\Delta(\mathcal{O}) = \boldsymbol{\varepsilon}_{\text{obs}}(\mathcal{O}) - \boldsymbol{\varepsilon}_u(\mathcal{O}). \tag{A10}$$

The conditioned field is then obtained by adding the kriging-like correction term,

$$\boldsymbol{\varepsilon}_c(\mathcal{U}) = \boldsymbol{\varepsilon}_u(\mathcal{U}) + \mathbf{C}_{\mathcal{U}\mathcal{O}}\, \mathbf{C}_{\mathcal{O}\mathcal{O}}^{-1}\, \Delta(\mathcal{O}), \tag{A11}$$

where $\mathbf{C}_{\mathcal{O}\mathcal{O}}$ is the block covariance among observed sites and $\mathbf{C}_{\mathcal{U}\mathcal{O}}$ is the cross-covariance between unobserved sites and observed sites. Under the nested LMC covariance above, and using the nugget convention, these blocks take the form

◦

$$\mathbf{C}_{\mathcal{O}\mathcal{O}} = \mathbf{P}_1 \otimes \mathbf{R}_{oo}^{(1)} + \mathbf{P}_2 \otimes \mathbf{R}_{oo}^{(2)} + \mathbf{P}_3 \otimes \mathbf{I}_{N_o}, \tag{A12}$$

$$\mathbf{C}_{\mathcal{U}\mathcal{O}} = \mathbf{P}_1 \otimes \mathbf{R}_{uo}^{(1)} + \mathbf{P}_2 \otimes \mathbf{R}_{uo}^{(2)}, \tag{A13}$$

where $\mathbf{R}_{oo}^{(\ell)}$ and $\mathbf{R}_{uo}^{(\ell)}$ are exponential correlation matrices computed from observation–observation and unobserved–observation distances for range R_ℓ, computed as in Eq. A2 The nugget $\mathbf{P}_3$ appears only in $\mathbf{C}_{\mathcal{O}\mathcal{O}}$ (variance at the same site), and not in $\mathbf{C}_{\mathcal{U}\mathcal{O}}$, consistent with independent nugget contributions across distinct sites.

Practical computation of $\boldsymbol{C}_{\mathcal{U}\mathcal{O}}\mathbf{C}_{\mathcal{O}\mathcal{O}}^{-1}\boldsymbol{\Delta}(\boldsymbol{\mathcal{O}})$

Directly forming and inverting $C_{\mathcal{O}\mathcal{O}}$ might be computationally expensive if N_o is large, moreover, the full matrix $\mathbf{C}_{\mathcal{U}\mathcal{O}}$ is usually very large. Instead, we compute the product $\mathbf{C}_{\mathcal{U}\mathcal{O}}\mathbf{C}_{\mathcal{O}\mathcal{O}}^{-1}\Delta(\mathcal{O})$ in two stages:

We first solve the linear system

$$\boldsymbol{C}_{\mathcal{O}\mathcal{O}} vec(\alpha^T) = vec(\Delta(\mathcal{O})^T), \tag{A14}$$

where $\alpha \in R^{N_o \times d}$ is an auxiliary matrix of "kriging weights" (one d-vector per observed site), and $vec(\cdot)$ stacks the columns of its argument. This equation makes the Kronecker structure explicit and fixes the ordering used in implementation. In practice we compute $vec(\alpha^T)$ by a Cholesky factorization of $\boldsymbol{C}_{\mathcal{O}\mathcal{O}}$. Specifically, we form an upper-triangular factor U such that $\boldsymbol{C}_{\mathcal{O}\mathcal{O}} \approx U^T U$, and then apply two triangular solves

$$U^T z = vec(\Delta(\mathcal{O})^T), Uvec(\alpha^T) = z. \tag{A15}$$

A small diagonal stabilization (jitter) may be added to $\boldsymbol{C}_{\mathcal{O}\mathcal{O}}$ if needed for numerical robustness. After solving for $vec(\alpha^T)$, we reshape to obtain α in site-major form.

Once α is known, the correction at the unobserved locations is computed using matrix multiplications that avoid forming the full $(N_u d) \times (N_o d)$ matrix $\boldsymbol{C}_{\mathcal{U}\mathcal{O}}$. Using the LMC decomposition,

$$\boldsymbol{C}_{\mathcal{U}\mathcal{O}} \boldsymbol{C}_{\mathcal{O}\mathcal{O}}^{-1} \Delta(\mathcal{O}) = \left(\boldsymbol{P}_1 \otimes \boldsymbol{R}_{uo}^{(1)} + \boldsymbol{P}_2 \otimes \boldsymbol{R}_{uo}^{(2)}\right) vec(\alpha^T). \tag{A16}$$

With the site-major representation $\alpha \in R^{N_o \times d}$, this product can be evaluated as

$$Adj(\mathcal{U}) = \left(\boldsymbol{R}_{uo}^{(1)} \alpha\right) \boldsymbol{P}_1{}^T + \left(\boldsymbol{R}_{uo}^{(2)} \alpha\right) \boldsymbol{P}_2{}^T, \tag{A17}$$

where $Adj(\mathcal{U}) \in R^{N_u \times d}$ is the deterministic correction added to the unconditional field. Finally,

$$\boldsymbol{\varepsilon}_c(\mathcal{U}) = \boldsymbol{\varepsilon}_u(\mathcal{U}) + Adj(\mathcal{U}). \tag{A18}$$

This two-stage computation is exactly what is implemented in the code: (i) solve a single linear system of size $N_o d$ to obtain α, and (ii) apply the cross-covariances from the unobserved points to the observed points through two dense multiplications $\boldsymbol{R}_{uo}^{(\ell)} \alpha$ followed by right-multiplication by P_ℓ^T. Finally, the conditioned ln-residual field and simulated ln-SAs are computed using Eq. A7.

Supporting figures

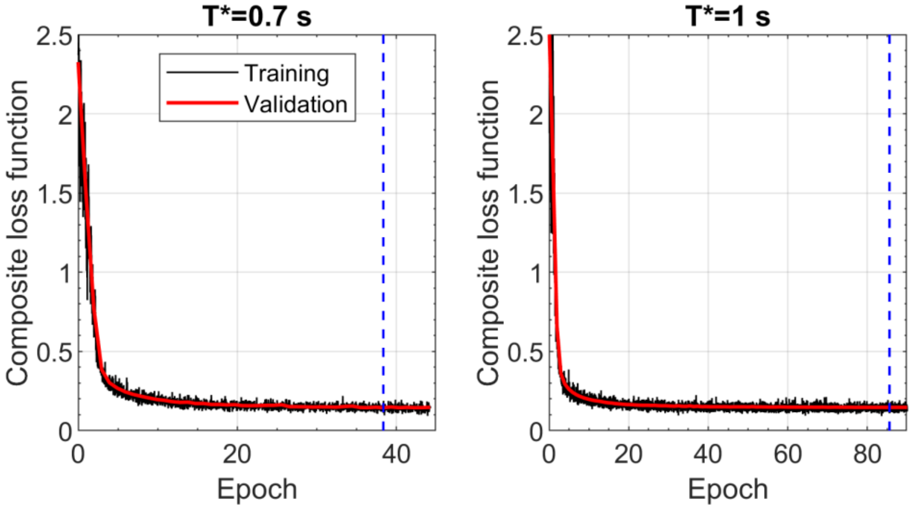

Figure S 1. Learning curves for ANNs (reference model) trained using as corner period T*=0.7 s (left), and T*=1 s (right). The blue dashed lines represent the epoch with the lowest validation loss which is the one selected.

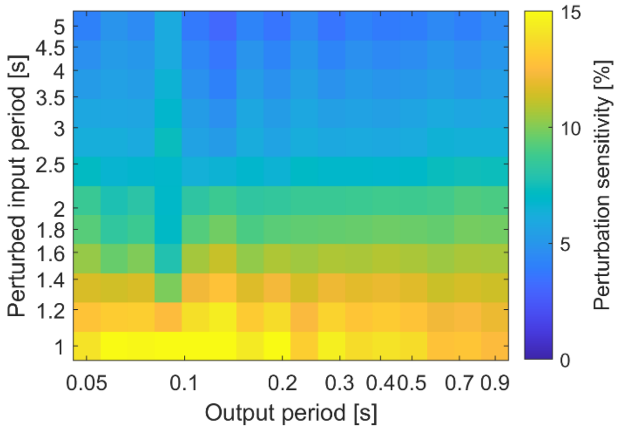

Figure S 2. Input-period perturbation sensitivity for one horizontal component of the ANN with T*=1 s. Each long-period input ordinate of one component was perturbed independently, and the RMS change in the predicted output spectrum was computed over the validation set. Values are normalized at each output period and expressed as percentage contributions to the total perturbation sensitivity.

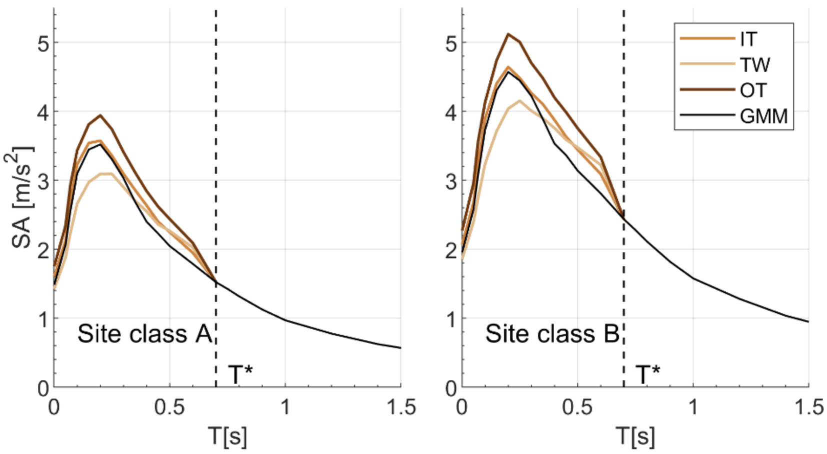

Figure S 3. Comparison of estimated horizontal response spectra for different regions by the ANN with T*=0.7 s. The source mechanism is normal faulting, M_w=6.5 and R_{JB}=10 km. EC8 site class is A on the left and B on the right. The input long-period spectra were obtained from the GMM by Lanzano et al. (2019).

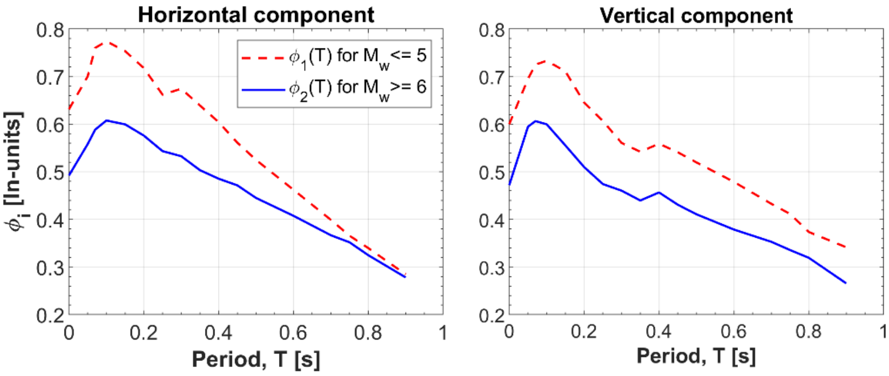

Figure S 4. Within-event standard deviations ϕ_1 and ϕ_2 from the heteroscedastic mixed-effects regression for all output periods for the ANN with T*=1 s.

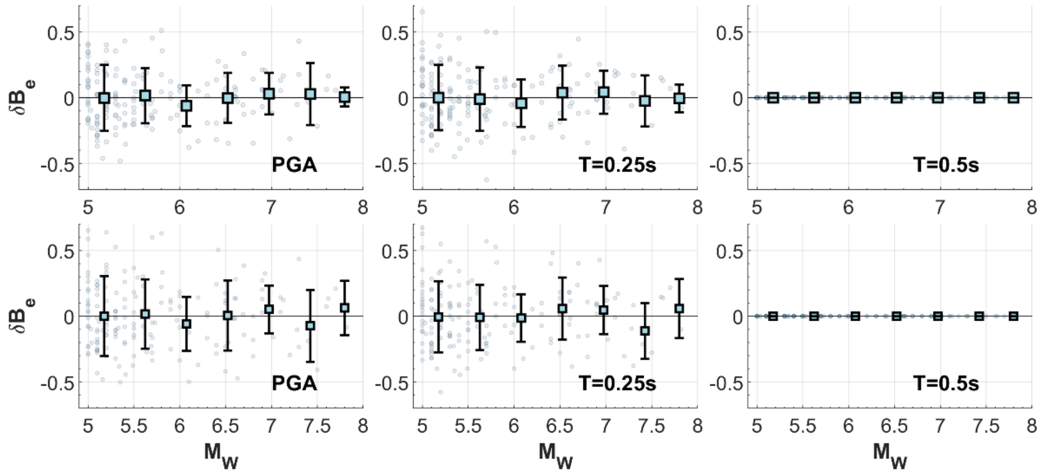

Figure S 5. Between-event residuals at various periods vs M_w for one horizontal component (top panel) and for the vertical component (lower panel). Error bars indicate ±1 standard deviation at various bins. T* corresponds to 1 s.

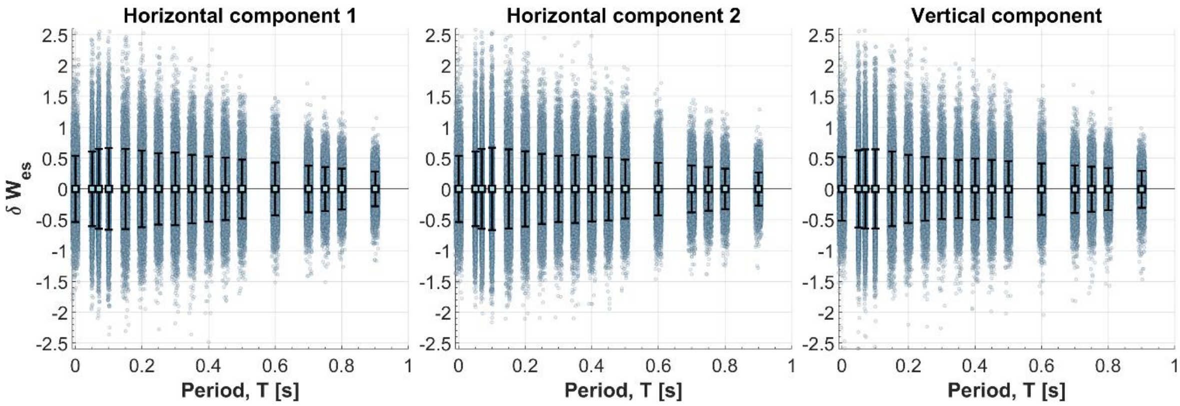

Figure S 6. Within-event residuals vs period for the three components. Points are plotted with a small horizontal jitter to reduce overlap and improve readability. Error bars indicate ±1 standard deviation. T* corresponds to 1 s. T* corresponds to 1 s.

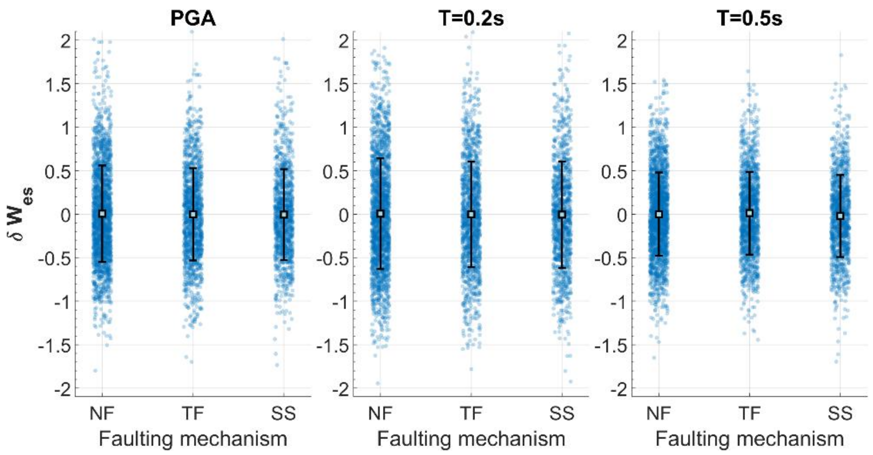

Figure S 7. Within-event residuals at various periods vs faulting mechanism for one horizontal component. Points are plotted with a small horizontal jitter to reduce overlap and improve readability. Error bars indicate ±1 standard deviation. T* corresponds to 1 s.

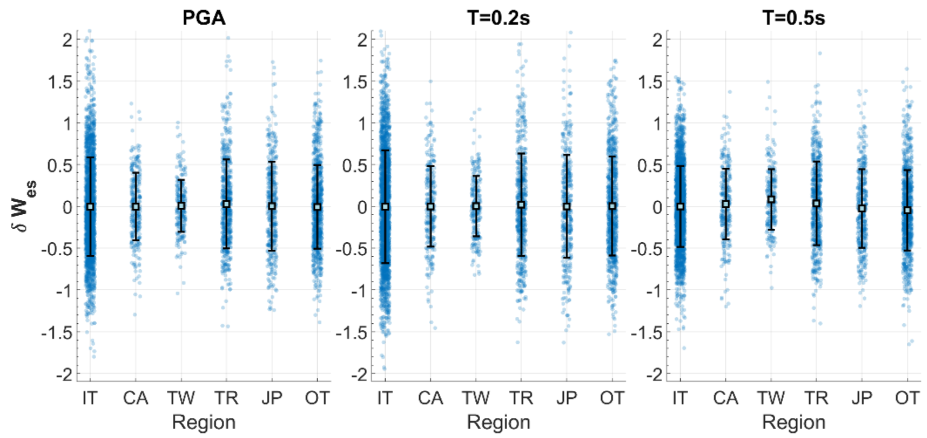

Figure S 8. Within-event residuals at various periods vs region for one horizontal component. Points are plotted with a small horizontal jitter to reduce overlap and improve readability. Error bars indicate ±1 standard deviation. T* corresponds to 1 s.

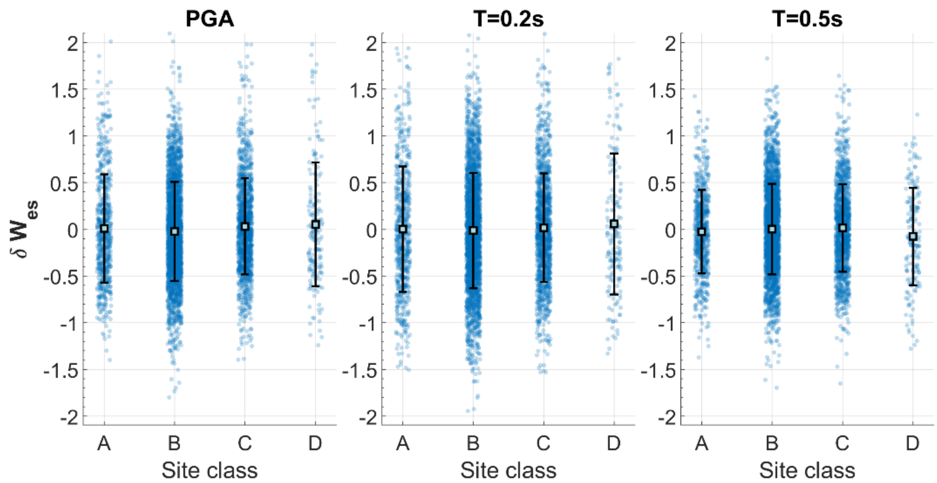

Figure S 9. Within-event residuals at various periods vs EC8 site class for one horizontal component. Points are plotted with a small horizontal jitter to reduce overlap and improve readability. Error bars indicate ±1 standard deviation. T* corresponds to 1 s.

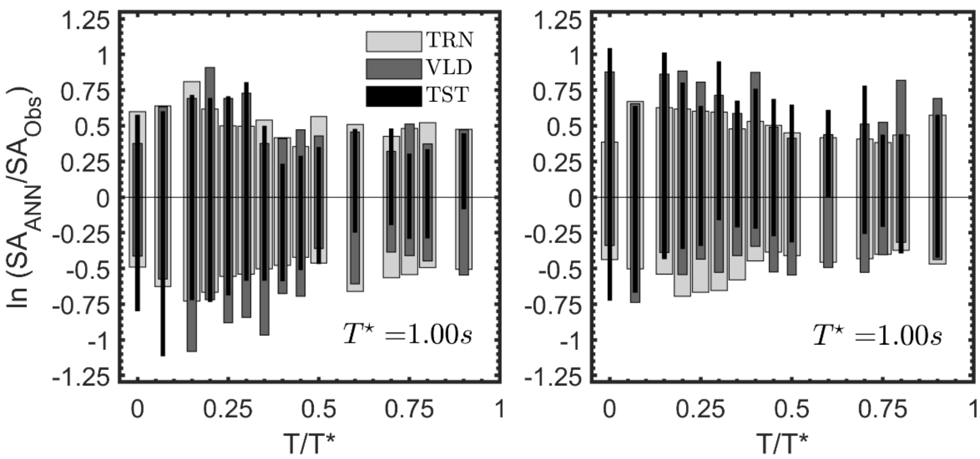

Figure S 10 Performance of two ANNs trained with the IceSMN dataset composed of 90 records, expressed in terms of error bars from the total logarithmic residuals for one horizontal component, i.e., ln(SA_{ANN}/SA_{Obs}), in which SA_{ANN} denotes the SA predicted by the ANN and SA_{Obs} are the observed ones. The performance is estimated at each vibration period T, here normalized with respect to the corner period T*=1 s. The residual patterns are not consistent across the three subsets, indicating an unstable calibration.

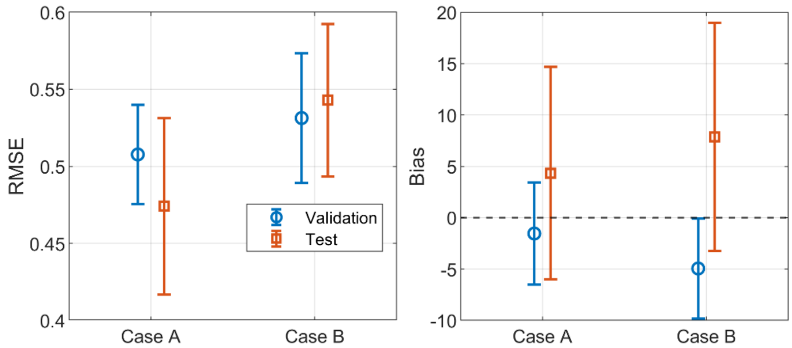

Figure S 11. Ablation test of the transfer-learning strategy using the local IceSMN dataset. Case A corresponds to the reference TL configuration, in which both the shared hidden layer and the output layers are updated during fine-tuning. Case B corresponds to a more restrictive configuration, in which only the output layers are updated. Symbols show the mean validation and test metrics over five independently trained networks, and error bars indicate the corresponding standard deviation. The reference configuration provides lower RMSE and lower absolute bias, indicating that updating the shared layer improves the calibration while maintaining stable generalization.

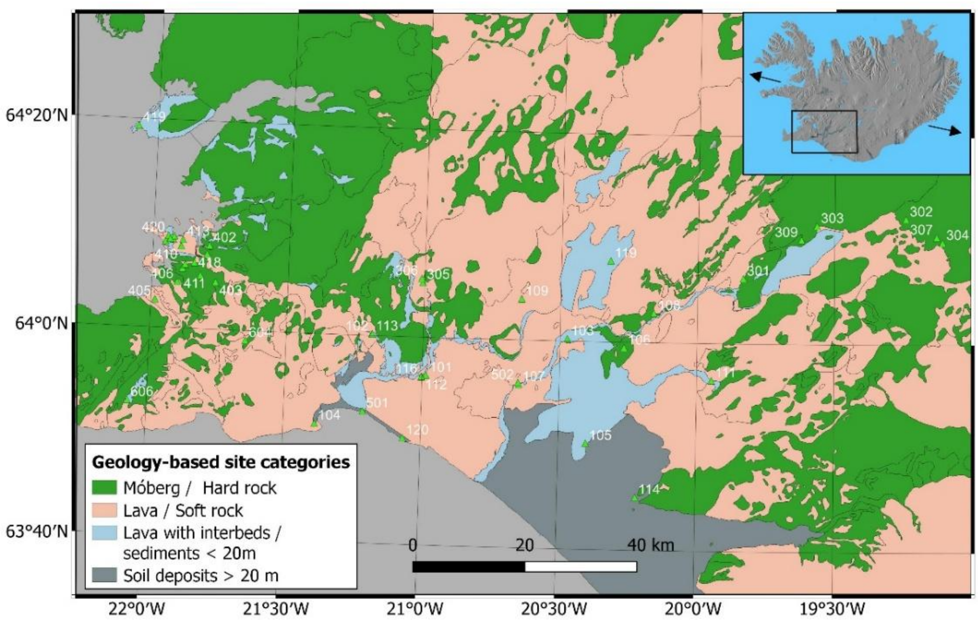

Figure S 12. Geology-based site classes used for training the ANN for Iceland.

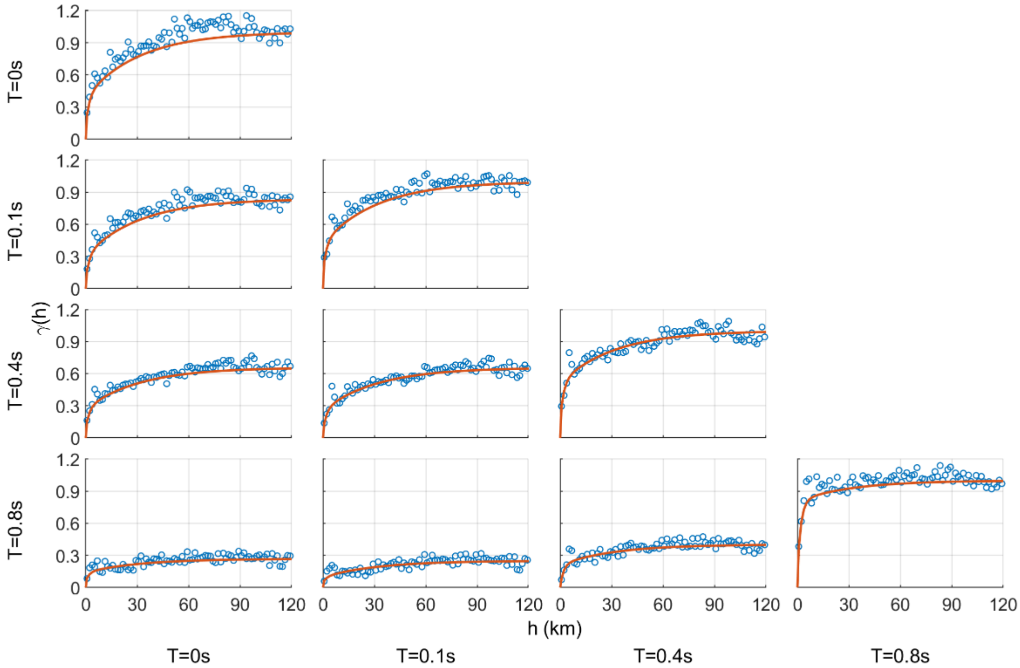

Figure S 13. Empirical semivariograms of within-event residuals and the fitted multivariate semivariogram model (solid lines) for the vertical component at period pairs for 0.0, 0.1, 0.4 and 0.7 s. Residuals are computed with respect to the prediction by the ANN with T*=1 s.

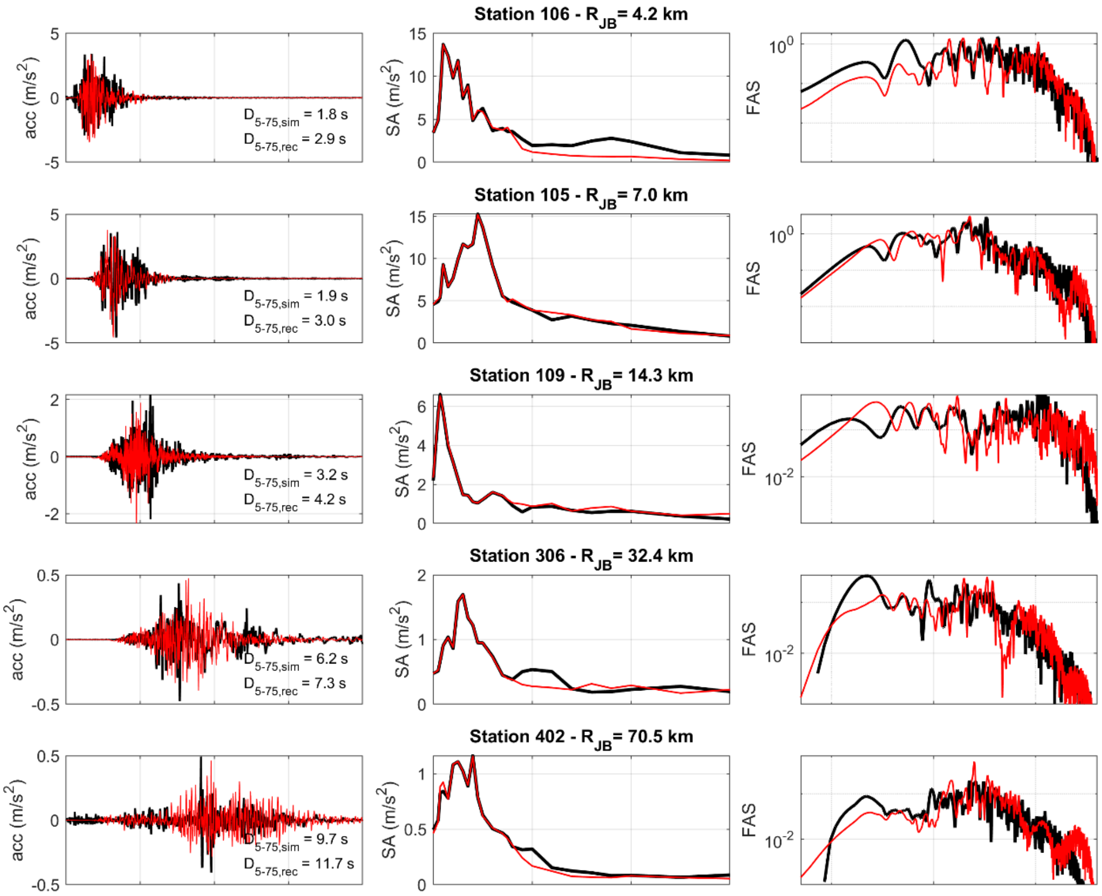

Figure S 14. Comparison of recorded and conditionally simulated BB accelerograms, SA, and Fourier amplitude spectra (FAS) at selected stations for the 17 June 2000 earthquake.

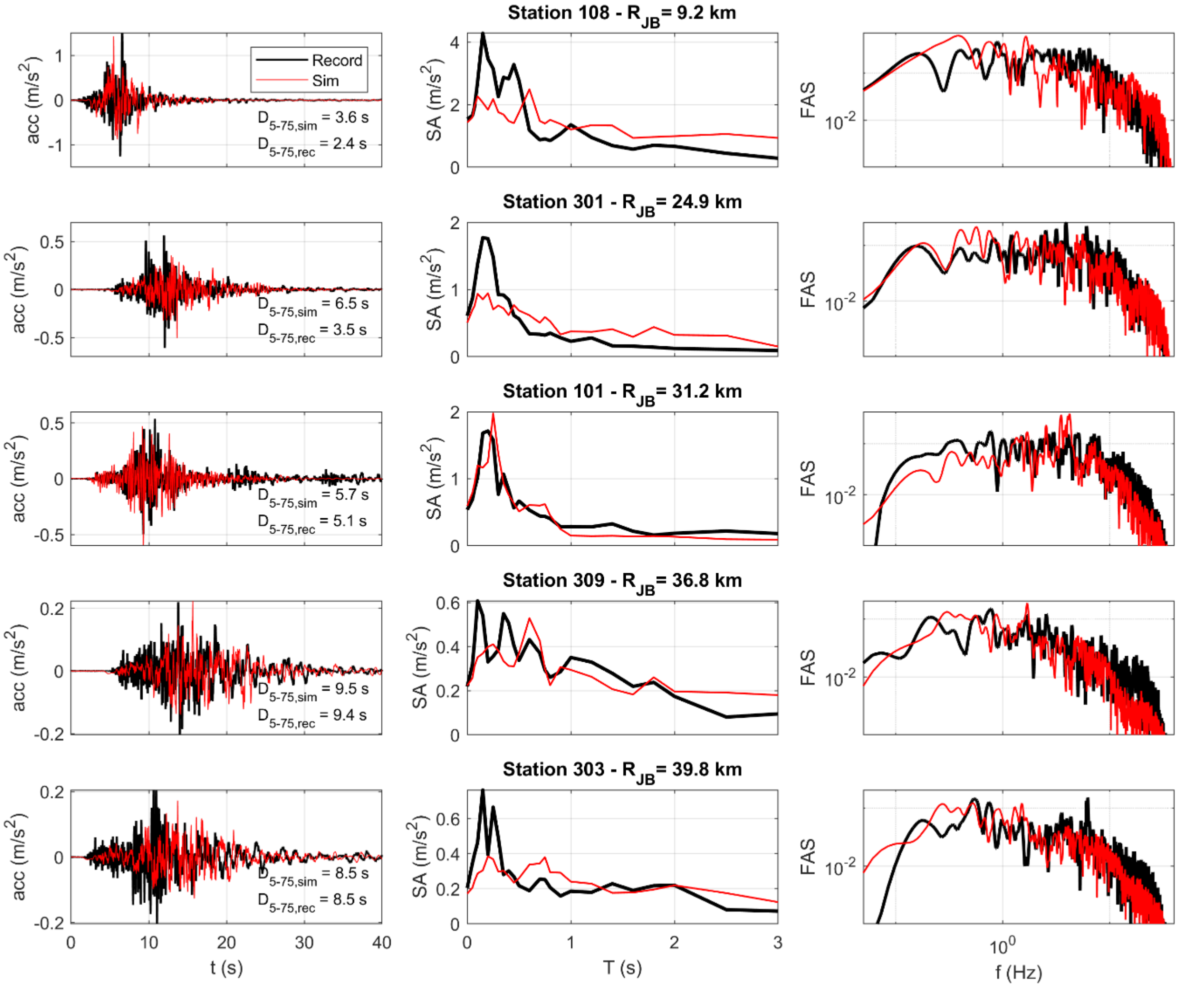

Figure S 15. Comparison of recorded and unconditionally simulated BB accelerograms, SA, and Fourier amplitude spectra (FAS) at the same stations shown in Figure 11.

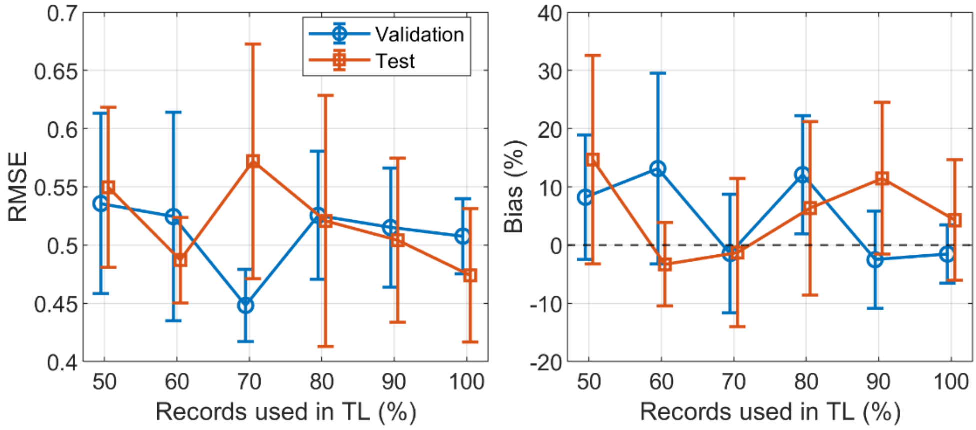

Figure S 16. Sensitivity of transfer-learning performance to the amount of target-region data used for fine-tuning. Five pretrained global ANNs were fine-tuned using progressively increasing fractions of the local Icelandic dataset. For each fraction, the symbols show the mean validation and test RMSE and bias; error bars indicate one standard deviation across the 5 ANNs. Both validation and test results show an overall reduction in RMSE and absolute bias as the fraction of local records increases, indicating that the regional calibration becomes more stable when more target-region data are included.